




# NATURE OF SUPERSONIC TURBULENCE AND DENSITY DISTRIBUTION FUNCTION IN THE MULTIPHASE INTERSTELLAR MEDIUM

MASATO I.N. KOBAYASHI <sup>1,2</sup> TSUYOSHI INOUE,<sup>3,4</sup> KENGO TOMIDA <sup>2</sup> KAZUNARI IWASAKI <sup>5</sup> AND  
HIROKI NAKATSUGAWA<sup>3</sup>

<sup>1</sup>*Division of Science, National Astronomical Observatory of Japan, 2-21-1 Osawa, Mitaka, Tokyo 181-8588, Japan*

<sup>2</sup>*Astronomical Institute, Graduate School of Science, Tohoku University, Aoba, Sendai, Miyagi 980-8578, Japan*

<sup>3</sup>*Division of Particle and Astrophysical Science, Graduate School of Science, Nagoya University, Aichi 464-8602, Japan*

<sup>4</sup>*Department of Physics, Konan University, Okamoto 8-9-1, Kobe, Japan*

<sup>5</sup>*Center for Computational Astrophysics, National Astronomical Observatory of Japan, Mitaka, Tokyo 181-8588, Japan*

(Received –; Revised –; Accepted –)

Submitted to ApJ

## ABSTRACT

Supersonic flows in the interstellar medium (ISM) are believed to be a key driver of the molecular cloud formation and evolution. Among molecular clouds' properties, the ratio between the solenoidal and compressive modes of turbulence plays important roles in determining the star formation efficiency. We use numerical simulations of supersonic converging flows of the warm neutral medium (WNM) resolving the thermal instability to calculate the early phase of molecular cloud formation, and investigate the turbulence structure and the density probability distribution function (density PDF) of the multiphase ISM. We find that both the solenoidal and compressive modes have their power spectrum similar to the Kolmogorov spectrum. The solenoidal (compressive) modes account for  $\gtrsim 80\%$  ( $\lesssim 20\%$ ) of the total turbulence power. When we consider both the cold neutral medium (CNM) and the thermally unstable neutral medium (UNM) up to  $T \lesssim 400$  K, the density PDF follows the log-normal distribution whose width  $\sigma_s$  is well explained by the known relation from the isothermal turbulence as  $\sigma_s = \ln(1 + b^2 \mathcal{M}^2)$  (where  $b$  is the parameter representing the turbulence mode ratio and  $\mathcal{M}$  is the turbulent Mach number). The density PDF of the CNM component alone ( $T \leq 50$  K), however, exhibits a narrower  $\sigma_s$  by a factor of  $\sim 2$ . These results suggest that observational estimations of  $b$  based on the CNM density PDF requires the internal turbulence within each CNM clump but not the inter-clump relative velocity, the latter of which is instead powered by the WNM/UNM turbulence.

*Keywords:* Interstellar medium, Warm neutral medium, Cold neutral medium, Interstellar dynamics

## 1. INTRODUCTION

Molecular clouds are progenitor of stars (Kennicutt & Evans 2012), and their physical states set the initial condition to determine the star formation rate/efficiency. In particular, the density structure is important where the densest volume of molecular clouds eventually collapse gravitationally to form stars (Krumholz & McKee 2005).

Corresponding author: Masato I.N. Kobayashi  
masato.kobayashi@nao.ac.jp, mskobayashi@astr.tohoku.ac.jp,  
masato.kobayashi@nagoya-u.jp

One of the key statistics is the (column) density probability distribution function (PDF). Based on analytic models and one-dimensional simulations, [Passot & Vázquez-Semadeni \(1998\)](#) show that isothermal turbulence produces a log-normal density PDF, which is a compilation of density enhancement by multiple shocks. Other analytic and numerical studies (e.g., [Padoan et al. 1997](#); [Nordlund & Padoan 1999](#)) also find such a log-normal density PDF and discuss its relation to the functional form of the stellar initial mass function (stellar IMF). Two- and three-dimensional simulations later suggest that the log-normal density PDF ubiquitously exists under the driven turbulence (e.g., [Federrath et al. 2008](#)), where the tails can deviate from the log-normal PDF due to non-isothermality ([Passot & Vázquez-Semadeni 1998](#); [Scalo et al. 1998](#)), self-gravity ([Klessen 2000](#)), and magnetization effects ([Li et al. 2008](#)) (see also the review by [Elmegreen & Scalo 2004](#)). Molecular clouds in the Milky Way galaxy indeed exhibit log-normal PDFs of (column) densities at low  $A_v$  regime, followed with a power-law tail at the high density end ([Lombardi et al. 2011](#); [Schneider et al. 2013](#); [Alves de Oliveira et al. 2014](#); [Schneider et al. 2016](#); but see also [Lombardi et al. 2015](#)).

There have been theoretical studies to estimate how the star formation rate varies based on the formation of the densest parts of such density PDFs within molecular clouds, by assuming some star formation efficiency (SFE) per free-fall time in individual molecular cloud cores (e.g., [Krumholz & McKee 2005](#); [Federrath et al. 2008](#); [Padoan & Nordlund 2011](#)). In particular, the suite of isothermal simulations with driven turbulence show that the turbulence mode ratio between solenoidal and compressive modes as well as the turbulent Mach number are important parameters that control the width of the density PDF (e.g., [Federrath et al. 2008, 2010](#)). For example, the star formation rate varies by a factor to one order of magnitude depending on the turbulence mode ratio ([Federrath & Klessen 2012](#)). This suggests that different density PDFs and the turbulence mode ratios result in various star formation rate of star-forming clouds even under a fixed turbulence power spectrum. Meanwhile, detailed simulations of radiative feedback from massive stars suggest that the SFE depends strongly on the initial column density of the cloud (e.g., [Kim et al. 2018](#); [Fukushima et al. 2020](#); [Fukushima & Yajima 2021](#)), and the turbulent structure likely impacts the stellar initial mass function as well ([Padoan & Nordlund 2002](#)). Therefore, it is important to reveal the turbulence structure and resultant density structures achieved in molecular clouds under realistic conditions of molecular cloud formation and evolution.

Supersonic flows in the interstellar medium (ISM) are one of the key driving sources of the turbulence. In galactic disk regions of star-forming galaxies (like the Milky Way galaxy), the typical interval between the passages of successive supersonic flows at any volume of the ISM is about 1 Myr ([McKee & Ostriker 1977](#)), where those flows originate in supernovae, expanding HII regions, galactic spirals etc.. The typical molecular cloud lifetime is also believed to be about a few 10 Myr, ([Kawamura et al. 2009](#); see also [Meidt et al. 2015](#)); where molecular clouds finally evaporate within 10 Myr due to the stellar feedback once massive stars form ([Hosokawa & Inutsuka 2006](#); [Kruijssen et al. 2019](#); [Fukushima et al. 2020](#); [Kim et al. 2021](#)). The interaction between molecular clouds and supersonic flows is naturally expected to occur multiple times during the cloud lifetime. [Matsumoto et al. \(2015\)](#) perform simulations of an isothermal ISM to investigate such interactions and show that the turbulent velocity within molecular clouds does not significantly differ between with and without the colliding flows if averaged over 1 – 3 free-fall time of the cloud (see also [Seifried et al. 2018](#)), but the turbulent mode ratio as well as the density PDF does differ, resulting in a rapid star formation due to the colliding flows. [Padoan et al. \(2016\)](#) perform simulations of multiple supernovae on a 100 pc scale and find that the expansion of multiple supernova remnants leads to drive the solenoidal modes stronger than the compressive modes by a factor of about 5.

Supersonic flows drive not only the turbulence but also the evolution of the thermal states by triggering the phase transition from the warm neutral medium (WNM) to the cold neutral medium (CNM) through the thermal instability (e.g., [Field 1965](#); [Balbus 1986](#)). This transition from the WNM to the CNM increases the density, and is believed to be an important first step of molecular cloud formation ([Koyama & Inutsuka 2002](#); [Audit & Hennebelle 2005](#)). Therefore, simultaneous investigations of both the turbulent structure and thermal states provide the comprehensive understanding of the evolution of the density structure within molecular clouds and resultant SFR. However, such studies are still limited and focus on the later stages of molecular cloud evolution where molecular clouds are massive enough to be self-gravitating (e.g., [Körtgen et al. 2017](#)).

As a complementary study to understand the molecular cloud evolution comprehensively from its early phase along with the thermal evolution, we perform hydrodynamics simulations of supersonic converging WNM flows, by resolving the thermal instability and the formation of the multi-phase ISM as a precursor of molecular clouds. We investigate the density PDF and turbulence

structure in this multi-phase ISM. We measure the turbulence power spectrum, velocity structure functions, CNM clump size and mass spectra, the density PDF as a function of temperature, and the turbulence mode ratio on 0.01 – 10 pc scales, based on which we show the range that the isothermal turbulence framework explains the density PDF in the multi-phase ISM.

The rest of this article is organized as follows. In Section 2, we explain the method of our simulations and analyses. In Section 3, we explain the basic equations that describe the density PDF and the known relation in the isothermal turbulence theory framework, as well as the definition of the solenoidal/compressive modes. We present the main results in Section 4 by using the data from the entire simulation domain, whereas we focus on the results from nine sub-volumes in Section 5. In Section 6, we discuss the implications from our results and future prospects. We summarize our results in Section 7, followed with Appendices explaining the convergence with respect to the spatial resolution and additional information of the technical details in our analyses.

## 2. METHOD

### 2.1. Basic Equations and Setups

We utilize the simulation code and setups from our previous study (Kobayashi et al. 2020). Our code is based on the hydrodynamics part from the magneto-hydrodynamics code originally developed in Inoue & Inutsuka (2008). This code employs the second-order Godunov scheme (van Leer 1979) and explicitly time-integrates the heating and cooling with the second order accuracy. We solve the following basic equations:

$$\frac{\partial \rho}{\partial t} + \nabla_i(\rho v_i) = 0, \quad (1)$$

$$\frac{\partial(\rho v_i)}{\partial t} + \nabla_j(P\delta_{ij} + \rho v_j v_i) = 0, \quad (2)$$

$$\frac{\partial e}{\partial t} + \nabla_i((e + P)v_i) = \nabla_i(\kappa(T)\nabla_i T) - \rho\mathcal{L}(T). \quad (3)$$

$\rho$  is the mass density,  $v$  represents the velocity,  $P$  represents the thermal pressure,  $T$  is the temperature, and  $\nabla_i = \partial/\partial x_i$ , where  $x_i$  spans  $x, y$ , and  $z$ .  $\delta_{ij}$  is the identity matrix. We calculate the total energy density,  $e$ , as  $e = P/(\gamma - 1) + \rho v^2/2$  where  $\gamma = 5/3$  is the ratio of the specific heat. We implement the thermal conductivity,  $\kappa$ , as  $\kappa(T) = 2.5 \times 10^3 T^{0.5} \text{ erg cm}^{-1} \text{ s}^{-1} \text{ K}^{-1}$ , representing collisions between hydrogen atoms (Parker 1953).

The thermal state of the gas is controlled by the balance between the cooling and heating, which is implemented in the net-cooling rate per mass  $\mathcal{L}(T)$ . We use the functional form of  $\mathcal{L}(T)$  that we develop in our pre-

vious study (Kobayashi et al. 2020). This is the combination of the results from Koyama & Inutsuka (2002) in  $T \leq 14,577 \text{ K}$  and Cox & Tucker (1969) and Dalgarno & McCray (1972) in  $T > 14,577 \text{ K}$  by considering the cooling rate due to Ly $\alpha$ , C II, He, C, O, N, Ne, Si, Fe, and Mg lines with the photo-electric heating, which corresponds to the typical ISM condition in the Milky Way galaxy. In general, the shock-heated WNM experiences the thermally unstable phase ( $(\partial(\mathcal{L}/T)/\partial T)_P < 0$ ; Balbus see e.g., 1986, 1995), leading to the formation of the CNM clumps. The multi-phase that appear in our simulations roughly correspond to the WNM as  $T \geq 5000 \text{ K}$ , the thermally unstable neutral medium (UNM) as  $100 \leq T < 5000 \text{ K}$ , and the CNM as  $T < 100 \text{ K}$  based on  $(\partial(\mathcal{L}/T)/\partial T)_P$ . We refer the readers to Kobayashi et al. (2020) for the exact form of this  $\mathcal{L}(T)$ .

We prepare a three-dimensional simulation domain with its size of  $L_{x,y,z} = 20, 10, 10 \text{ pc}$ , and calculate the head-on collision of supersonic WNM converging flows continuously injected through the two  $x$  boundaries over 3 Myr. We employ the periodic boundary condition on both  $y$  and  $z$  boundaries. This flow creates a shock-compressed layer sandwiched by two shock fronts at the box center  $x \simeq L_x/2$  where the two flows collide. The flow velocity is fixed as  $20 \text{ km s}^{-1}$  representing common situations in galactic disks (e.g., the late phase of supernova remnant expansion, H II region expansion, and normal shocks due to galactic spirals). The injected WNM flow is thermally stable with the mean number density  $n_0 = 0.57 \text{ cm}^{-3}$  and pressure  $P_0/k_B = 3500 \text{ K cm}^{-3}$ . This corresponds to the mean temperature of  $6141 \text{ K}$ , the sound speed of  $C_s = 8.16 \text{ km s}^{-1}$ , and the ram pressure of the converging flow as  $P/k_B = 2.6 \times 10^4 \text{ K cm}^{-3}$ .

The density of the injected WNM flow has a fluctuation with the Kolmogorov power spectrum  $P_\rho(k) \propto k^{-11/3}$  (Kolmogorov 1941; Armstrong et al. 1995). The highest frequency is  $k/2\pi = 12.5 \text{ pc}^{-1}$  (i.e., the wavelength of  $0.08 \text{ pc}$ ). The amplitude is set such that the mean dispersion is  $\sqrt{\langle \delta n_0^2 \rangle}/n_0 = 1$  as the most realistic parameter in our calculation to describe the density structure in star-forming regions (Kobayashi et al. 2020). The interaction between this density inhomogeneity and shock fronts induces turbulence in the shock-compressed layer (e.g., Inoue & Inutsuka 2012; Carroll-Nellenback et al. 2014).

We employ uniform spatial resolution of  $0.01 \text{ pc}$  in fiducial analyses, with additional resolutions of  $0.02 \text{ pc}$ ,  $0.04 \text{ pc}$ ,  $0.08 \text{ pc}$  for comparison (Appendix A). This  $0.01 \text{ pc}$  is motivated by our previous systematic study over a wide parameter range of  $\sqrt{\langle \delta n_0^2 \rangle}/n_0$  by Kobayashi et al. (2020). In Kobayashi et al. (2020), we show that, with the thermal instability, the spatial resolution with

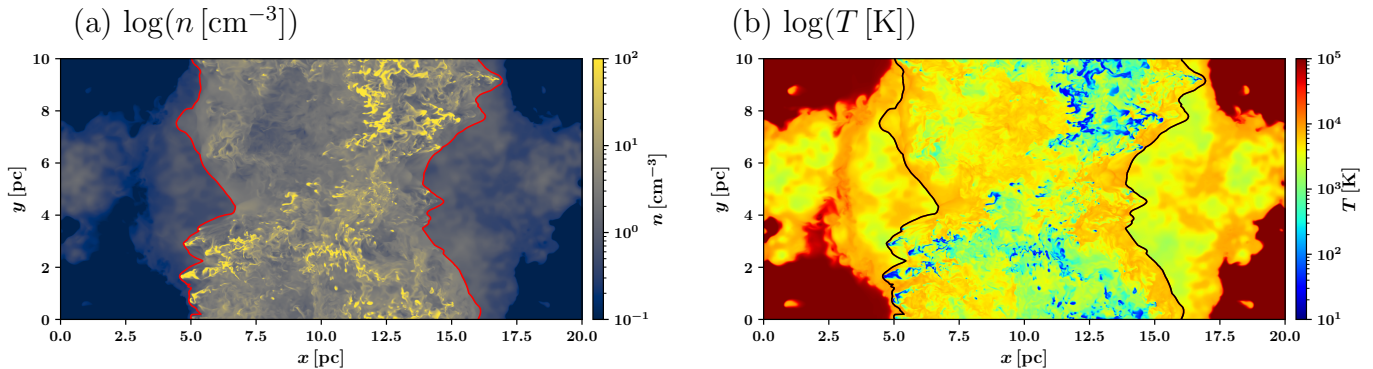


**Figure 1.** Panel (a): The density map from our three-dimensional simulation at 2.5 Myr. The central volume sandwiched by two shock fronts (thin red curves) is the progenitor of molecular clouds, within which the multi-phase ISM forms. Panel (b): Same as (a) but the temperature map with the shock positions shown as thin black curves.

$\lesssim 0.02$  pc is required to fully resolve the cooling length of the UNM and have the convergence in the mean density of the shock-compressed layer. This spatial resolution resolves the highest frequency of the injected density fluctuation with at least eight cells. In Appendix A, we also show that CNM clump properties have their convergence with the 0.01 pc resolution compared with 0.02 pc and 0.04 pc (such as mean density, size and mass spectra).

The calculation results are sampled every 0.1 Myr, and we identify the shock front position by  $P > 1.3P_0$  to define the shock-compressed layer in each sampled time. Figure 1 shows an example of the two-dimensional slices of the density distribution (Panel (a)) and the temperature distribution (Panel (b)) at 2.5 Myr. The central region sandwiched by the two shock fronts is the progenitor of molecular clouds, within which the multi-phase ISM forms through the thermal instability. The effective typical cooling length peaks at  $\sim 1$  pc for the UNM and at 0.02–0.2 pc for the CNM (see Panel (a) of Figure 10). Therefore, through the growth of the thermal instability, the CNM structures develop on sub-pc scales as seen as clumpy structures on  $\sim 0.1$  pc in Figure 1.

### 2.2. The Decomposition into the Solenoidal and Compressive Modes and Our Choice of Analyzed Volume

We apply the Fourier transformation to the shock-compressed layer to obtain the Fourier component of the velocity field by using the Fast Fourier Transform in the West (FFTW 3.3; Frigo & Johnson 2005), and decompose this into the solenoidal modes and compressive modes (see Section 3). We perform this decomposition both on the entire volume of the shock-compressed layer and on nine sub-volumes of  $(2.56 \text{ pc})^3$  size within the shock-compressed layer. We summarize the technical details involved in this decomposition in Appendix B.

We employ five temperature thresholds to extract volumes with various thermal states and investigate the difference in the turbulent structure and density PDF between the WNM+UNM and CNM;  $T \leq 50$  K,  $T \leq 200$  K,  $T \leq 400$  K,  $T \leq 600$ , and  $T \leq 1000$  K.

### 3. DENSITY PDF IN ISOTHERMAL TURBULENCE

The log-normal density PDF is defined as

$$p_s(s) = \frac{1}{\sqrt{2\pi\sigma_s^2}} \exp\left(-\frac{(s-s_0)^2}{2\sigma_s^2}\right), \quad (4)$$

where  $s$  is the natural logarithm of density. In the framework of the isothermal turbulence, essentially three parameters determine the star formation rate by controlling the fraction of dense volume that gravitationally collapse to form stars. One is the mean density, another is the mean Mach number of turbulence, and the other is the mode ratio between the solenoidal/compressive modes. In the case of such isothermal turbulence, it is known that the width of this log-normal density PDF  $\sigma_s$ , is well described by the combination of the forcing parameter  $b$  and the mean Mach number  $\mathcal{M}$  as

$$\sigma_{s,\text{theory}}^2 = \ln(1 + b^2 \mathcal{M}^2), \quad (5)$$

(see e.g., Federrath et al. 2010).  $b$  represents the compressibility defined by the compressive ratio  $\chi$  (Pan et al. 2016) as:

$$b = \sqrt{\frac{\chi}{1 + \chi}}, \quad (6)$$

$$\chi = \frac{\langle \tilde{\mathbf{v}}_{\text{comp}}^2 \rangle}{\langle \tilde{\mathbf{v}}_{\text{sol}}^2 \rangle}. \quad (7)$$

Here  $\tilde{\mathbf{v}}_{\text{comp}}$  and  $\tilde{\mathbf{v}}_{\text{sol}}$  mean the compressive and solenoidal modes of the turbulent velocity field, respectively.

Any velocity field is in principle able to be decomposed into the solenoidal (transverse) and compressive (longitudinal) modes through the Helmholtz decomposition as:

$$\tilde{\mathbf{v}}_{\text{sol}}(\hat{\mathbf{k}}) = (\hat{\mathbf{k}} \times \tilde{\mathbf{v}}) \times \hat{\mathbf{k}} \quad (8)$$

$$\tilde{\mathbf{v}}_{\text{comp}}(\hat{\mathbf{k}}) = (\hat{\mathbf{k}} \cdot \tilde{\mathbf{v}}) \hat{\mathbf{k}}. \quad (9)$$

Here  $\hat{\mathbf{k}}$  is a unit wave vector and  $\tilde{\mathbf{v}}$  is the Fourier component of the velocity field. In the following analyses, we will measure  $b$ ,  $\mathcal{M}$ , and  $\sigma_s$  from our simulations, and evaluate  $\sigma_{s,\text{theory}}$  based on Equation 5 to investigate the difference between  $\sigma_s$  and  $\sigma_{s,\text{theory}}$  in various thermal states.

#### 4. RESULTS I: THE ENTIRE VOLUME OF THE SHOCK-COMPRESSED LAYER

Hereafter, the spatial frequency  $k/2\pi$  denotes the inverse of the wavelength of a corresponding wave, such that  $k/2\pi = 0.1 \text{ pc}^{-1}$  corresponds to 10 pc.

##### 4.1. Solenoidal and Compressive Mode Fraction

Panel (a) in Figure 2 shows the one-dimensional averaged velocity power spectrum. The overall spectrum follows the Kolmogorov spectrum  $\propto k^{-5/3}$  where the solenoidal modes dominate than the compressive mode on all scales. The spectrum of the solenoidal modes exhibit a break at  $k/2\pi \sim 5.0 \text{ pc}^{-1}$  so does the total spectrum. This is attributed to the numerical diffusion, which we evaluate further in Appendix A. Given that the typical cooling length of the UNM peaks at  $\sim 1 \text{ pc}$  (Panel (a) of Figure 10 in Appendix A) and that the break of the compressive mode power is limited compared with that of the solenoidal mode power, our spatial resolution is high enough to resolve the cooling length of the UNM to follow the dynamical condensation through the thermal instability (but also see Section 6.2).

Panel (b) in Figure 2 shows the solenoidal/compressive mode fraction out of the total turbulent power. This shows that the solenoidal modes account for 80–90 % on most scales.

Figure 3 shows the time-evolution of the total solenoidal/compressive mode fraction integrated from  $k/2\pi = 0.1$  to  $5.12 \text{ pc}^{-1}$  over the entire volume of the shock-compressed layer. A converging flow configuration itself is a compressive motion and thus the compressive mode initially exists  $\sim 40 \%$ . Along with the turbulent generation, the solenoidal modes increase to reach 80–90 %. After 0.5 Myr, the fractions into the solenoidal and compressive modes are quasi-steady

with 80–90 % and 10–20 %, respectively. In this quasi-steady state, the mass fraction between WNM, UNM, and CNM is also steady, and the expansion speed of the shock-compressed layer is almost constant (Kobayashi et al. 2020). At the final timestep, 3 Myr, the fraction of the compressive and solenoidal modes are  $f_{\text{comp}} = 0.10$  and  $f_{\text{sol}} = 0.90$  respectively. The corresponding mode ratio  $\chi$  becomes 0.11 so that the forcing parameter is  $b = 0.32$ .

##### 4.2. Density PDF and its Width with Various Thermal States

Panel (a) of Figure 4 shows the thermal state within the shock-compressed layer at 3 Myr. This shows that the shock-heated WNM at  $n = 1\text{--}10 \text{ cm}^{-3}$  and  $T \sim 6000 \text{ K}$  cools through the thermally unstable regime, and their densest parts reach the CNM state at  $100\text{--}1000 \text{ cm}^{-3}$  and  $T \lesssim 50 \text{ K}$ . The wide distribution on this phase diagram realizes due to the combination of the turbulent mixing and the thermal instability. For example, if the converging flow is a completely one-dimensional head-on collision as  $\sqrt{\langle \delta n_0^2 \rangle} / n_0 = 0$ , the medium cools with the constant pressure set by the ram pressure of the converging flow (along with the black dashed line on Panel (a) of Figure 4).

Panel (b) of Figure 4 shows the density PDF, overplotted with the corresponding log-normal fittings<sup>1</sup>. Table 1 summarizes the measured properties. The mean sound speed and the mean velocity dispersion are evaluated as

$$\langle C_s(T_t) \rangle = \frac{\sum_{T(\mathbf{x}) \in T_t} \sqrt{\gamma P(\mathbf{x}) / \rho(\mathbf{x})}}{\sum_{T(\mathbf{x}) \in T_t}}, \quad (10)$$

$$\sqrt{\langle \delta v^2(T_t) \rangle} = \sqrt{\frac{\sum_{T(\mathbf{x}) \in T_t} (\mathbf{v}(\mathbf{x}) - \bar{\mathbf{v}})^2}{\sum_{T(\mathbf{x}) \in T_t}}}. \quad (11)$$

Here  $T(\mathbf{x}) \in T_t$  indicates that we select cells whose temperature satisfies the temperature thresholds of  $T_t$ . For this  $T_t$  thresholds, we select  $T \leq 50 \text{ K}$ ,  $T \leq 200 \text{ K}$ ,  $T \leq 400 \text{ K}$ ,  $T \leq 600$ , and  $T \leq 1000 \text{ K}$ , to cover the transition from the UNM down to the CNM. We derive the mean Mach number as  $\langle \mathcal{M}(T_t) \rangle = \sqrt{\langle \delta v^2(T_t) \rangle} / \langle C_s(T_t) \rangle$ .  $\sigma_{s,\text{sim}}$  shows the width of the fitted log-normal distribution. We also obtain  $\sigma_{s,\text{theory}}$  by inserting the measured  $b = 0.32$  and  $\langle \mathcal{M} \rangle$  into Equation 5 (Section 4.1).

<sup>1</sup> Note that, although the histograms are well fitted by log-normal functions, the heating/cooling processes always induce deviation from the log-normal functions because the temperature and density in the thermally-stable state have correlations. For example, the density PDF of  $T < 50 \text{ K}$  has a strong transition at  $50\text{--}100 \text{ cm}^{-3}$ , where the thermally-stable state has  $T = 50 \text{ K}$  so that most of the gas with  $T < 50 \text{ K}$  is restricted to  $n \gtrsim 100 \text{ cm}^{-3}$  (see Panel (a) of Figure 4).

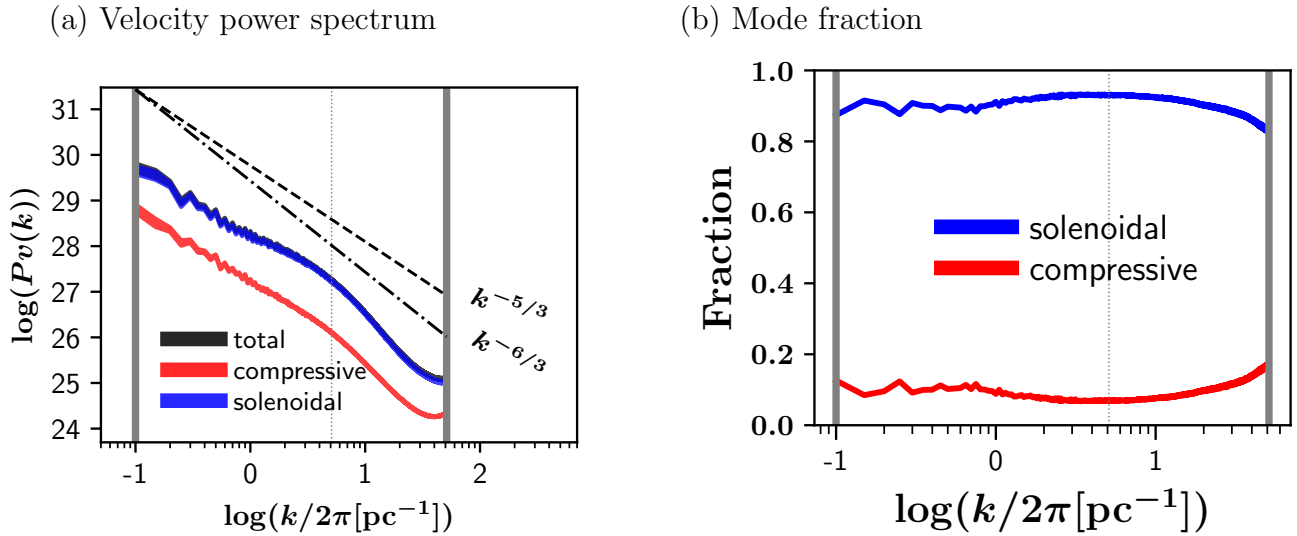


**Figure 2.** Panel (a): The one-dimensional averaged velocity power spectrum at 3 Myr over the entire volume of the shock-compressed layer. The black line corresponds to the total power whereas the colored lines show the breakdown as the solenoidal modes (blue) and the compressive modes (red). The solenoidal mode amounts to  $\gtrsim 80\%$  of the total power on all scales (shown in Panel (b)), so that the “total” (black) is almost overlapped with “solenoidal” (blue) in this figure. The shade shows the Poisson noise based on the sample counts in each  $k$ -vector bin. The vertical gray lines show  $k/2\pi = 0.1 \text{ pc}^{-1}$  (left solid; the proxy of the lowest frequency of the shock-compressed layer (see Appendix B)),  $k/2\pi = 5.12 \text{ pc}^{-1}$  (middle thin dotted: the numerical diffusion likely impacts the power on  $k/2\pi > 5.12 \text{ pc}^{-1}$ ), and the Nyquist frequency  $k/2\pi = 51.2 \text{ pc}^{-1}$  (right solid). We use the powers on  $0.1 \text{ pc}^{-1} \leq k/2\pi \leq 5.12 \text{ pc}^{-1}$  in the analyses hereafter. We overplot two reference lines representing power-laws of  $\propto k^{-5/3}$  and  $k^{-6/3}$ . The  $k$ -space is linearly binned where the highest frequency corresponds to the Nyquist frequency. Panel (b): Same as Panel (a) but the solenoidal/compressive mode fraction out of the total turbulent power.

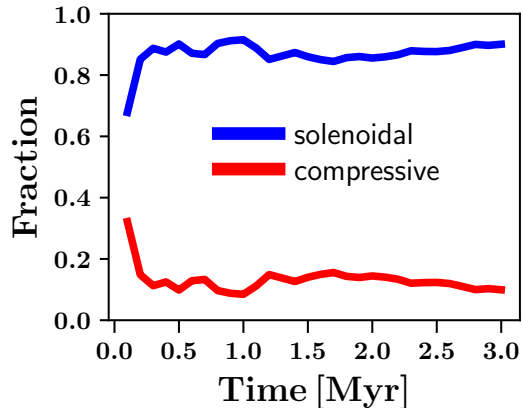


**Figure 3.** The time evolution of the solenoidal/compressive mode fraction integrated over the entire volume of the shock-compressed layer. The blue (red) line shows the solenoidal (compressive) modes. We calculate the sum of the modes on  $0.1 \text{ pc}^{-1} \leq k/2\pi \leq 5.12 \text{ pc}^{-1}$  to evaluate the fractions. At the finale timestep, 3 Myr, the fraction of the compressive and solenoidal modes are  $f_{\text{comp}} = 0.10$  and  $f_{\text{sol}} = 0.90$  respectively. The corresponding mode ratio  $\chi$  becomes 0.11 so that the forcing parameter is  $b = 0.32$ .

Note that measuring  $b$  within individual temperature thresholds is difficult, especially cold components that

are spatially disconnected (see Figure 1). Nevertheless, in Section 4.2.2, we will utilize the velocity field in the real space to measure the numerical-grid-scale turbulence mode fraction and show that the fraction of the compressive (solenoidal) mode powers are 23% (77%). This is still solenoidal-mode dominated and is similar to the averaged  $b = 0.32$  that we obtain here on the entire shock-compressed layer. In this section, therefore, we simply employ  $b = 0.32$  for all the temperature ranges when evaluating  $\sigma_{\text{s,theory}}$ .

Table 1 shows that 1) the measured width of the density PDF  $\sigma_{\text{s,sim}}$  and the expected width  $\sigma_{\text{s,theory}}$  are close to each other when we combine both the UNM and CNM components, especially at  $T < 400 \text{ K}$ , 2) but the difference becomes larger towards the higher temperature range ( $T < 1000 \text{ K}$ ) and the lower temperature range ( $T < 50 \text{ K}$ ) up to a factor of  $\sim 2$ . The difference is attributed to the evaluation of  $b$  and  $\mathcal{M}$  in  $\sigma_{\text{s,theory}}$  (see Equation 5). In the following subsections, we will show that  $\sigma_{\text{s,sim}}$  and  $\sigma_{\text{s,theory}}$  are close to each other when we take into account the thermal states properly to select the consistent  $\langle C_s(T_t) \rangle$ ,  $\sqrt{\langle \delta v^2(T_t) \rangle}$  and  $\sigma_{\text{s,sim}}$  responsible for each other, thus the difference between  $\sigma_{\text{s,sim}}$  and  $\sigma_{\text{s,theory}}$  is a natural consequence of the multi-phase nature of this system.

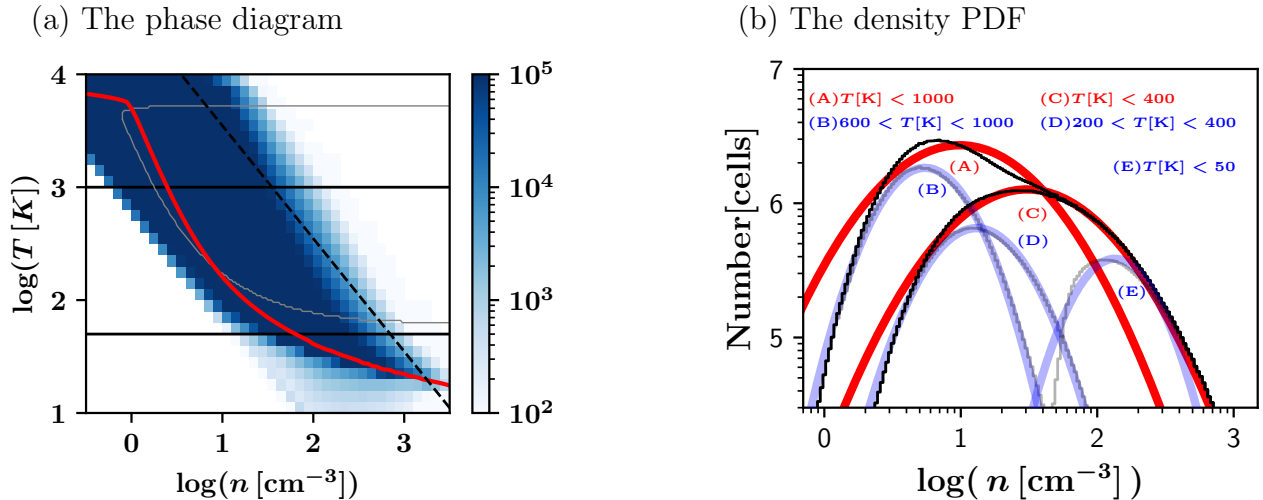


**Figure 4.** Panel (a): The cell histogram on the temperature-density diagram at 3 Myr. The color is coded as  $\log(\text{Cells})$ . The grey thin curve encloses the thermally unstable region with  $(\partial(\mathcal{L}/T)/\partial T)_P < 0$  (Balbus 1986, 1995). The red thick curve shows the thermal equilibrium state. The two horizontal black lines correspond to  $T = 1000$  K and  $T = 50$  K. The black dashed line shows the temperature corresponding to the ram pressure of the converging flow. Panel (b): The volume-weighted density PDF (i.e., cell histogram) and its fitted log-normal function of the entire volume of the shock-compressed layer at 3 Myr. We plot five histograms and corresponding log-normal functions based on temperature thresholds;  $T[\text{K}] \leq 1000$  (left red),  $600 < T[\text{K}] \leq 1000$  (left blue),  $T[\text{K}] \leq 400$  (middle red),  $200 < T[\text{K}] \leq 400$  (middle blue),  $T[\text{K}] \leq 50$  (right blue).

**Table 1.** Measured properties from the entire volume of the shock-compressed layer at 3 Myr

|   | $f_{\text{comp}}$  | $f_{\text{sol}}$    | $\chi$              | $b$                 |                      |
|---|--------------------|---------------------|---------------------|---------------------|----------------------|
|   | 0.10               | 0.90                | 0.11                | 0.32                |                      |
|   | $T[\text{K}] < 50$ | $T[\text{K}] < 200$ | $T[\text{K}] < 400$ | $T[\text{K}] < 600$ | $T[\text{K}] < 1000$ |
| $\langle C_s \rangle \text{ [km s}^{-1}\text{]}$                        | 0.65               | 0.98                | 1.31                | 1.64                | 2.25                 |
| $\sqrt{\langle \delta v^2 \rangle} \text{ [km s}^{-1}\text{]}$          | 3.93               | 4.23                | 4.43                | 4.62                | 4.98                 |
| $\mathcal{M} = \sqrt{\langle \delta v^2 \rangle} / \langle C_s \rangle$ | 6.02               | 4.31                | 3.37                | 2.82                | 2.21                 |
| $\sigma_{\text{s,sim}}$   | 0.61               | 0.96                | 1.12                | 1.22                | 1.13                 |
| $\sigma_{\text{s,theory}}$  | 1.24               | 1.02                | 0.87                | 0.76                | 0.63                 |

**Note.** The top row: the compressive mode fraction  $f_{\text{comp}}$ , the solenoidal mode fraction  $f_{\text{sol}}$ , the mode ratio  $\chi$ , and the forcing parameter  $b$ . The middle row: The top line shows the temperature threshold. The second line,  $\langle C_s \rangle$ , corresponds to the mean sound speed and the third line,  $\langle \sigma_v \rangle$ , corresponds to the velocity dispersion (see Equations 10 and 11). The fourth line,  $\mathcal{M}$ , is the effective Mach number based on  $\langle C_s \rangle$  and  $\langle \sigma_v \rangle$ . The fifth line,  $\sigma_{\text{s,sim}}$ , is the width of the density PDF from our simulations.

The sixth line,  $\sigma_{\text{s,theory}}$ , is the width of the density PDF expected from the isothermal turbulent theory, inserting  $b = 0.315$  and  $\mathcal{M}$  (the fourth line) into Equation 5.

#### 4.2.1. Warmer Region with $T \sim 1000$ K

In the warmer regions,  $\sigma_{\text{s,sim}}$  is wider than  $\sigma_{\text{s,theory}}$ .  $\sqrt{\langle \delta v^2(T_i) \rangle}$  and  $\langle C_s(T_i) \rangle$  are volume-weighted quantities so that they tend to depend more on diffuse (i.e., warmer) components when we expand the temperature threshold to the warmer regime. For example,  $\sigma_{\text{s,theory}}$  at  $T < 1000$  K depends more on WNM and UNM at  $T \sim 1000$  K that just starts to cool. On the other hand, the measured  $\sigma_{\text{s,sim}}$  tries to take into account the cooler

UNM and CNM components as well ( $T < 400$  K), so that  $\sigma_{\text{s,sim}}$  at  $T < 1000$  K is wider than  $\sigma_{\text{s,theory}}$ <sup>2</sup>.

In Panel (b) of Figure 4, we additionally show the breakdown of density PDF, such as  $600 < T[\text{K}] < 1000$

<sup>2</sup> The total density PDF of the whole temperature range is bimodal between WNM and CNM, which can be seen in the thick black histogram in Panel (b) of Figure 4 labeled “(A)”. The log-normal fitting is close to the peak of warmer components that have more volume than the cold components.

(labeled as (B)) and  $200 < T[\text{K}] < 400$  (labeled as (D)). If we restrict ourselves to the distribution (B) alone, we find that  $\sigma_{s,\text{sim}}(600 < T[\text{K}] < 1000) = 0.629$ . Meanwhile  $\langle C_s(600 < T[\text{K}] < 1000) \rangle = 2.96 \text{ km s}^{-1}$  and  $\sqrt{\langle \delta v^2(600 < T[\text{K}] < 1000) \rangle} = 4.10 \text{ km s}^{-1}$ , so that  $\mathcal{M}(600 < T[\text{K}] < 1000) = 1.39$  and  $\sigma_{s,\text{theory}}(600 < T[\text{K}] < 1000) = 0.51$ . This shows that  $\sigma_{s,\text{sim}}$  and  $\sigma_{s,\text{theory}}$  is closer to each other at  $600 < T[\text{K}] < 1000$  rather than at the entire  $T[\text{K}] < 1000$ , suggesting that the original values of  $\sqrt{\langle \delta v^2 \rangle}$ ,  $\langle C_s \rangle$ ,  $\mathcal{M}$  and corresponding  $\sigma_{s,\text{theory}}$  at  $T < 1000$  K is weighted to warmer components.

#### 4.2.2. Cold Region with $T < 50\text{K}$ : CNM Clump Statistics

Contrarily to the warmer regimes,  $\sigma_{s,\text{theory}}$  is wider than  $\sigma_{s,\text{sim}}$  at colder regimes. In  $T < 50$  K, for example,  $b \simeq 0.1$  is required to have  $\sigma_{s,\text{sim}} = \sigma_{s,\text{theory}}$  with the given  $\mathcal{M} = 5.99$ . Such a small  $b$  less than 0.3 is difficult to achieve in reality even with a purely solenoidal turbulence (Federrath et al. 2008). Figure 2 already indicated that Kolmogorov spectrum extends to smaller scales with the almost constant  $b \sim 0.3$ , even when we perform simulations with a higher resolution to remove the numerical diffusion effect. The generation of the compressive mode due to the thermal instability also takes place on small scales. Therefore, our results suggest that the evaluation of  $\mathcal{M}$  plays a more significant role to explain the difference between  $\sigma_{s,\text{sim}}$  and  $\sigma_{s,\text{theory}}$ . As seen in Section 2.1, the sub-pc-scale CNM clumps form through the thermal instability and they are spatially disconnected to each other. Our straightforward evaluation of  $\sqrt{\langle \delta v^2(T_t) \rangle}$  Equation 11, therefore reflects the relative velocity between CNM clumps more than the internal velocity dispersion within individual CNM clumps.

To further confirm the above discussions, we identify CNM clumps and measure their physical properties. We define a CNM clump as a connected volume with the temperature  $T < 50$  K, which typically has its density  $n \gtrsim 50 \text{ cm}^{-3}$  (see Panel (a) of Figure 4). In the following analyses, we restrict ourselves to the clumps with  $\geq 512$  cells to reduce the effect of numerical noises, and analyze 2403 such CNM clumps.

Panels (a) and (b) of Figure 5 show the size and mass histograms at 3 Myr. We use  $\sqrt{I_{\text{max}}/M}$  as the size of individual clumps, where each clump has  $I_{\text{max}}$  as the maximum eigenvalue of its inertia matrix and  $M$  as its mass. The size and mass peaks at  $\sim 0.08$  pc and  $6 \times 10^{-3} M_{\odot}$ . The volume-weighted mean density of a

clump<sup>3</sup> is  $\langle n_{\text{clump}} \rangle_V \simeq 189 \text{ cm}^{-3}$ . As the mass spectrum of the CNM clumps is  $dn/dm \propto m^{-1.8}$ , more massive clumps dominate the mass budget of CNM components. This spectrum is often reported by other authors investigating converging flows (e.g., Inoue & Inutsuka 2012) and consistent with a theoretically expected spectrum of  $dn/dm \propto m^{-1.78}$  under the thermal instability growth (see e.g., Hennebelle & Audit 2007).

Panel (c) of Figure 5 shows the relation between the size and internal velocity dispersion within each CNM clump at 3 Myr. The mean internal velocity dispersion and the mean sound speed are  $\sqrt{\langle (\delta v^2)_{\text{clump}} \rangle_V} = 1.05 \text{ km s}^{-1}$  and  $\langle C_{s,\text{clump}} \rangle_V = 0.43 \text{ km s}^{-1}$ , so that the mean Mach number within CNM clumps is  $\mathcal{M}_{\text{clump}} \sim 2.44$ . This internal velocity dispersion is consistent with  $\lesssim 1 \text{ km s}^{-1}$  suggested from the second-order velocity structure function on the 0.1 pc scale (shown later in Section 5.2 as Figure 8).

In order to evaluate the mode parameter within CNM clumps,  $b_{\text{clump}}$ , we measure the powers of the grid-scale turbulent modes as  $\langle (\nabla_{\mathbf{g}} \cdot \mathbf{v})_{\text{clump}}^2 \rangle_V$  for the compressive mode and  $\langle (\nabla_{\mathbf{g}} \times \mathbf{v})_{\text{clump}}^2 \rangle_V$  for the solenoidal mode (Kida & Orszag 1990a,b). Here  $\mathbf{v}$  is the velocity field in the real space,  $\nabla_{\mathbf{g}}$  is the spatial differential operator on each numerical cell scale. The fraction of the compressive (solenoidal) mode powers are 23 % (77 %), and the corresponding mode parameter on the grid-scale within CNM clumps is  $b_{\text{clump}} \sim 0.48$ .  $b_{\text{clump}}$  is, therefore, indeed larger than 0.1 as we speculated in the first paragraph of this subsection.  $b_{\text{clump}} \sim 0.48$  also suggests that the mode fraction at the Nyquist frequency alone in the Fourier analysis (the grey vertical line in Panel (a) of Figure 2) already indicated a fraction close to  $b_{\text{clump}}$  even though such a Fourier power is dominated rather by the WNM and UNM than by the CNM.

Equation 5 with  $\mathcal{M}_{\text{clump}} \sim 2.44$  and  $b_{\text{clump}} \sim 0.48$  expects that the density PDF width of the CNM component alone is  $\sigma_{s,\text{theory}} \simeq 0.61$ , which is consistent with  $\sigma_{s,\text{sim}} = 0.61$ .

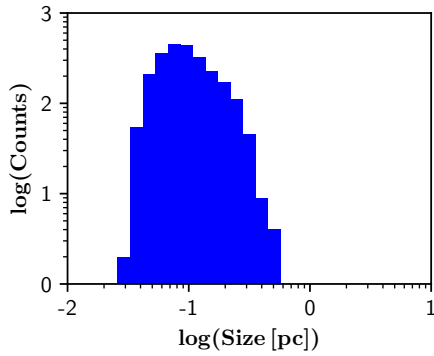
In conclusion of Sections 4.2.1 and 4.2.2, our results suggest that 1) when we focus on the volume with  $T < 1000$  K, turbulence is more powered by diffuse warm components, such as the WNM and UNM that

<sup>3</sup> Hereafter, we use the subscript ‘‘clump’’ as the volume-weighted mean within each clump, and  $\langle \rangle_V$  as the mean over all clumps weighted with each clump’s volume. For example of  $\langle n_{\text{clump}} \rangle_V$ , we first measure the volume-weighted mean density of  $i$ -th clump,  $n_{\text{clump},i}$ , then obtain the overall volume-weighted mean density as  $\langle n_{\text{clump}} \rangle_V = \sum_i n_{\text{clump},i} V_i / \sum_i V_i$ . Here,  $V_i$  is the volume of  $i$ -th clump and  $i$  spans all CNM clumps.

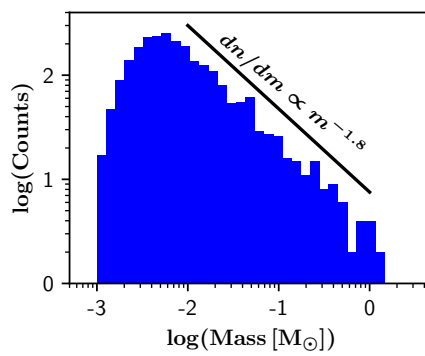


## CNM clump statistics

(a) Size histogram



(b) Mass histogram



(c) Size - velocity dispersion relation

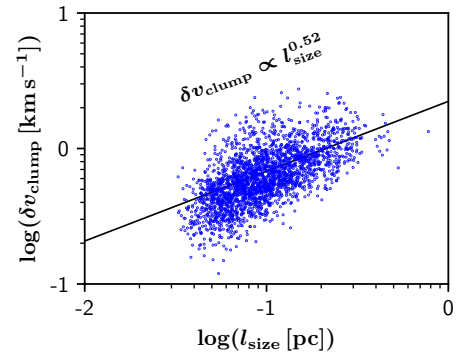


**Figure 5.** The statistics of 2403 CNM clumps: Panel (a) shows the size histogram, Panel (b) shows the mass histogram, and Panel (c) shows the size - internal velocity dispersion relation at 3 Myr. In Panel (c), each small circle represents individual CNM clumps and the black solid line is the least-square fitting result, which is  $\delta v_{\text{clump}} \propto l_{\text{size}}^{0.52}$ .

just start to cool<sup>4</sup>, thus the isothermal theory with the volume-weighted turbulence explains the width of the density PDF of such warmer components without the cold tails, 2) the coldest part of the density PDF ( $T < 50$  K) is governed by the turbulence within individual CNM clumps than by the strong turbulence on the entire cloud scale, which determines the relative velocity between CNM clumps. The turbulent  $\mathcal{M}$  within individual CNM clumps is more important to evaluate the density PDF of the CNM component alone, and 3) Equation 5 from the isothermal theory is directly applicable when we compile all the volumes with  $T < 400$  K.

## 5. RESULTS II: THE SUB-VOLUMES OF THE SHOCK-COMPRESSED LAYER

In this section, we analyze nine sub-volumes to investigate the local variations. The nine sub-volumes are selected so that their volume-centered position is  $(L_x/2, L_y/2, L_z/2)$  for the most-centered one, and  $(L_x/2 \pm 2.56 \text{ pc}, L_y/2 \pm 2.56 \text{ pc}, L_z/2 \pm 2.56 \text{ pc})$  for the other eight ones. We assume the periodicity in the Fourier analysis, and also expect that the boundary condition does not significantly affect the turbulent powers on the scales of  $k/2\pi \leq 5.12 \text{ pc}^{-1}$  (c.f., Section B.2).

### 5.1. Turbulence Modes and Density PDF

Panel (a) of Figure 6 shows the averaged velocity power spectrum from the nine sub-volumes, with the minimum and maximum range measured among the sub-volumes. Albeit the wavelength range affected by

the numerical diffusion have a significant fraction in these sub-volumes, the overall power spectrum shows the Kolmogorov spectrum and the solenoidal modes always dominate the turbulence power, similar to the result of the entire volume of the shock-compressed layer (Section 4.1). Panel (b) of Figure 6 shows the time-evolution of the solenoidal and compressive modes, which shows that, at later stages of  $\gtrsim 1.7$  Myr, the variation among the nine regions is  $\lesssim 10\%$  and the solenoidal modes amount to  $\sim 80\%$  of the total turbulence power<sup>5</sup>. At the final timestep, 3 Myr, the fraction of the compressive and solenoidal modes are  $f_{\text{comp}} = 0.15$  and  $f_{\text{sol}} = 0.85$  respectively.  $\chi$  becomes 0.18 so that the forcing parameter is  $b = 0.39$ .

Figure 7 shows the sum of the density PDF from the nine sub-volumes, overplotted with the corresponding log-normal fittings. We summarize the measured properties on the Table 2. Similar to Table 1,  $\sigma_{\text{s, sim}}$  and  $\sigma_{\text{s, theory}}$  are comparable when we combine both the UNM and CNM components, especially at  $T \lesssim 400$  K.

In conclusion, the power spectrum and the density PDF suggest that the local variation of the mode fraction exists but limited at about a 10 percent level so that the solenoidal modes are always dominant.

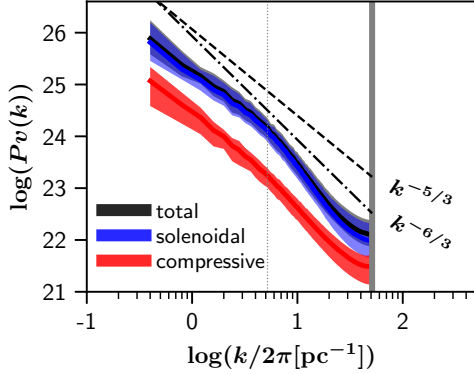
### 5.2. Second-Order Velocity Structure Function

To investigate the connection between the various thermal states in our simulations and the observations of the ISM turbulence, we measure the second-order velocity structure function within individual temperature

<sup>4</sup> Inoue & Inutsuka (2012) also reported similar properties where the power of WNM and UNM turbulence is stronger than that of the CNM in their molecular cloud formation simulations in the magnetized medium.

<sup>5</sup> Note that the significant variation at early phases is likely affected by the choice of analyzed volume, so that focusing on only after 1 Myr is fair when we discuss the variation between the sub-volumes; see Section B.2.

(a) Velocity power spectrum



(b) Mode fraction

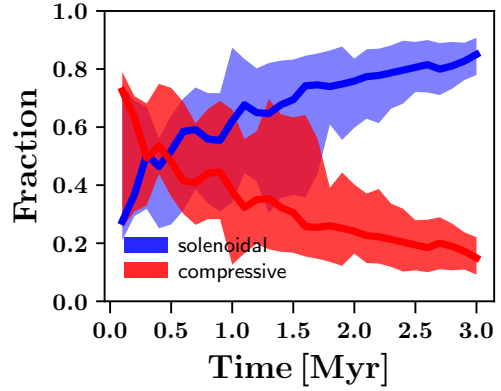


**Figure 6.** Panel (a): The velocity power spectrum compiled from the nine sub-volumes of the shock-compressed layer at 3 Myr. The color represents the turbulence mode (black for the total, blue for the solenoidal modes, and red for the compressive modes). The shade corresponds to the minimum and maximum range of each mode among the sub-volumes. The thick colored lines within each shade shows the mean of the nine sub-volumes. The vertical gray lines show the Nyquist frequency  $k/2\pi = 51.2 \text{ pc}^{-1}$  (right solid), and  $k/2\pi = 5.12 \text{ pc}^{-1}$  (middle thin dotted: the numerical diffusion likely impacts the power on  $k/2\pi > 5.12 \text{ pc}^{-1}$ ). We overplot two reference lines representing power-laws of  $\propto k^{-5/3}$  and  $k^{-6/3}$ . Panel (b): The time evolution of the solenoidal/compressive mode fraction compiled over nine sub-volumes. The blue (red) line shows the solenoidal (compressive) modes. We utilize the powers in on  $0.39 \text{ pc}^{-1} \leq k/2\pi \leq 5.12 \text{ pc}^{-1}$  for the analysis of the turbulent mode fraction. The shade corresponds to the minimum and maximum range among the sub volumes.

**Table 2.** Mean measured properties from the nine sub-volumes of the shock-compressed layer at 3 Myr

|   | $f_{\text{comp}}$       | $f_{\text{sol}}$        | $\chi$                  | $b$                     |                         |
|---|-------------------------|-------------------------|-------------------------|-------------------------|-------------------------|
|   | 0.15                    | 0.85                    | 0.18                    | 0.39                    |                         |
|   | $T[\text{K}] \leq 50$   | $T[\text{K}] \leq 200$  | $T[\text{K}] < 400$     | $T[\text{K}] < 600$     | $T[\text{K}] < 1000$    |
| $\langle C_s \rangle [\text{km s}^{-1}]$                                | 0.65 $^{+0.02}_{-0.01}$ | 1.01 $^{+0.05}_{-0.06}$ | 1.37 $^{+0.10}_{-0.10}$ | 1.70 $^{+0.14}_{-0.14}$ | 2.32 $^{+0.24}_{-0.20}$ |
| $\sqrt{\langle \delta v^2 \rangle} [\text{km s}^{-1}]$                  | 2.40 $^{+1.44}_{-0.44}$ | 2.75 $^{+1.44}_{-0.64}$ | 2.98 $^{+1.39}_{-0.70}$ | 3.19 $^{+1.34}_{-0.76}$ | 3.61 $^{+1.20}_{-0.88}$ |
| $\mathcal{M} = \sqrt{\langle \delta v^2 \rangle} / \langle C_s \rangle$ | 3.66 $^{+2.23}_{-0.76}$ | 2.72 $^{+1.33}_{-0.63}$ | 2.17 $^{+0.87}_{-0.50}$ | 1.87 $^{+0.61}_{-0.44}$ | 1.56 $^{+0.33}_{-0.39}$ |
| $\sigma_{\text{s,sim}}$   | 0.54 $^{+0.10}_{-0.14}$ | 0.85 $^{+0.12}_{-0.17}$ | 1.04 $^{+0.12}_{-0.14}$ | 1.11 $^{+0.14}_{-0.13}$ | 1.02 $^{+0.24}_{-0.17}$ |
| $\sigma_{\text{s,theory}}$  | 1.05 $^{+0.31}_{-0.30}$ | 0.86 $^{+0.25}_{-0.28}$ | 0.73 $^{+0.21}_{-0.25}$ | 0.65 $^{+0.17}_{-0.23}$ | 0.55 $^{+0.13}_{-0.21}$ |

**Note.** Same as Table 1 but for the mean from the nine sub-volumes within the shock-compressed layer. The  $\pm$  shows the maximum/minimum range around the mean value.

thresholds:

$$S(r) = \langle |\mathbf{v}(\mathbf{x} + \mathbf{r}) - \mathbf{v}(\mathbf{x})|^2 \rangle, \quad (12)$$

where  $r = |\mathbf{r}|$ . This analysis does not require any stringent boundary condition compared with the power spectrum analysis, and is capable of directly analyzing individual thermal states even when the volume of the focused thermal states are clumpy and spatially disconnected to each other. For example, the structure function of CNM component alone can cover from the turbulence within CNM clumps to the relative motion between CNM clumps on 10 pc scales. However, the

internal velocity dispersion are affected by the numerical diffusion as we have discussed so far. Therefore, let us focus on only large scales  $\gtrsim 0.2 \text{ pc}$  when we have quantitative discussions in the following.

Figure 8 shows the measured structure function. As a representative of different thermal states, we employ  $T < 50 \text{ K}$ ,  $200 \text{ K} < T < 400 \text{ K}$ , and  $600 \text{ K} < T < 1000 \text{ K}$  similar to the density PDF analyses. The analyzed volume in each panel of Figure 8 is limited to the one within the corresponding temperature range, so that Panel (a) represents the CNM and Panels (b) and (c) mostly represent the UNM. We overplot the power-laws of Kol-

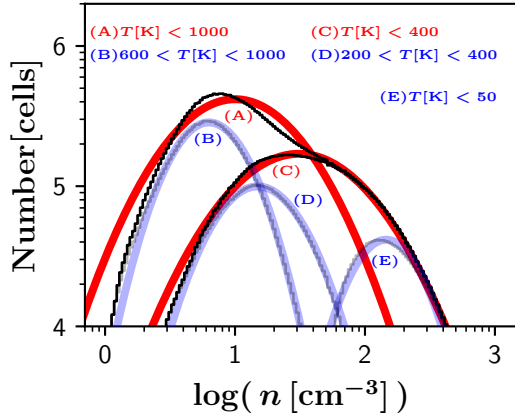


**Figure 7.** The volume-weighted density PDF (histogram) and its fitted log-normal function of the nine sub-volumes at 3 Myr.

mogorov ( $S(r) \propto r^{2/3}$ ) and Larson ( $S(r) \propto r^1$ ). The figure indicates that the UNM components exhibit the spectrum close to the Kolomogorov (e.g.,  $600 < T[\text{K}] < 1000$ ), while the CNM components exhibit the spectrum close to the Larson (e.g.,  $T < 50$  K). Therefore, the early phase of molecular cloud formation through converging flows exhibits the Larson’s law in the CNM components, which is consistent with observed supersonic turbulence (e.g., Larson 1981; Heyer & Brunt 2004) while the overall turbulence follows the Kolomogorov spectrum. Note that, even in more evolved phases, molecular clumps formed by the converging flow exhibit the Larson type size-velocity dispersion relation (e.g., Inoue & Inutsuka 2012).

These results suggest that, if we observationally measure the density PDF and the second-order velocity structure function in multiple thermal states, they can be utilized to test our understanding of molecular cloud formation controlled both by the turbulence and the thermal evolution shown in this article, and provide estimations of the turbulent forcing parameter  $b$  more consistent with the thermal evolution of molecular clouds.

## 6. DISCUSSIONS

### 6.1. Comparison with Previous Studies and the Importance of Self-gravity

We calculate up to 3 Myr and the accumulated mass is limited to  $2.6 \times 10^3 M_\odot$ . We ignore the self-gravity, which is sub-dominant compared with the ram pressure of the converging flow and the thermal/turbulent energy until  $\sim 40$  Myr (c.f., Kobayashi et al. 2020). Our calculation therefore corresponds to early phases of the cloud formation and evolution.

Compared with our simulations, other previous studies focus on more later stages of the cloud evolution and show the impact of the self-gravity. For example, Matsumoto et al. (2015) perform hydrodynamics simulations to calculate 3 Myr evolution of an isothermal molecular cloud, whose initial mean density (mass) is already  $10^2 - 10^3 \text{ cm}^{-3}$  ( $10^3 - 10^4 M_\odot$ ) and whose initial turbulence is with the solenoidal modes alone. They report that the compressive mode fraction remains  $\lesssim 20$  percent without the self-gravity, which is close to our value of 10 percent, while the compressive mode generation due to the self-gravity is able to enhance the fraction more than 20 percent. Körtgen et al. (2017) also perform cloud formation simulations with heating and cooling similar to our studies, but focus more on massive clouds ( $\sim 10^5 M_\odot$ ) on larger scale (256 pc). They investigate a long-term evolution (until 30 Myr) by employing a refinement technique with the spatial resolution from 62 pc to 0.03 pc at highest, and measure the turbulent driving parameter  $b$ . Their results show that the parameter  $b$  evolves from 0.3 to 0.8 due to the self-gravitational collapse of the cloud.

Our current results of  $b \sim 0.3$  is consistent with the early stages of these previous studies. It is, however, still important to investigate the evolution of self-gravitating clouds by resolving the thermal instability coherently from the beginning to later stages  $\sim 40$  Myr. This is left for future studies.

### 6.2. Limitations: Internal Velocity Dispersion of CNM Clumps

In Section 4.2.2, we show that, to determine the density PDF of the CNM component, the internal velocity dispersion in individual CNM clumps is more responsible than the relative velocity between the CNM clumps. Higher resolution is still ideal to perform a more precise quantitative comparison between  $\sigma_{s,\text{sim}}$  and  $\sigma_{s,\text{theory}}$ , because the  $\sigma_s$  dependence on the Mach number comes in with  $\mathcal{M}^2$  as shown in Equation 4, and also because the spatially-smallest growing mode of the thermal instability is limited by the size of numerical cells and our current calculations are affected by the numerical diffusion on the scales below CNM clumps  $\lesssim 0.1$  pc. Such calculations are left for future studies but we expect that this will be important when compared with (future) observations (see Section 6.4).

Nevertheless, our current simulations already obtained the mean power of the internal turbulence good enough to discuss its importance on the density PDF. In Appendix A, we will investigate the resolution dependence to show that our current simulation with 0.1 pc resolution has the convergence. For example, the inter-

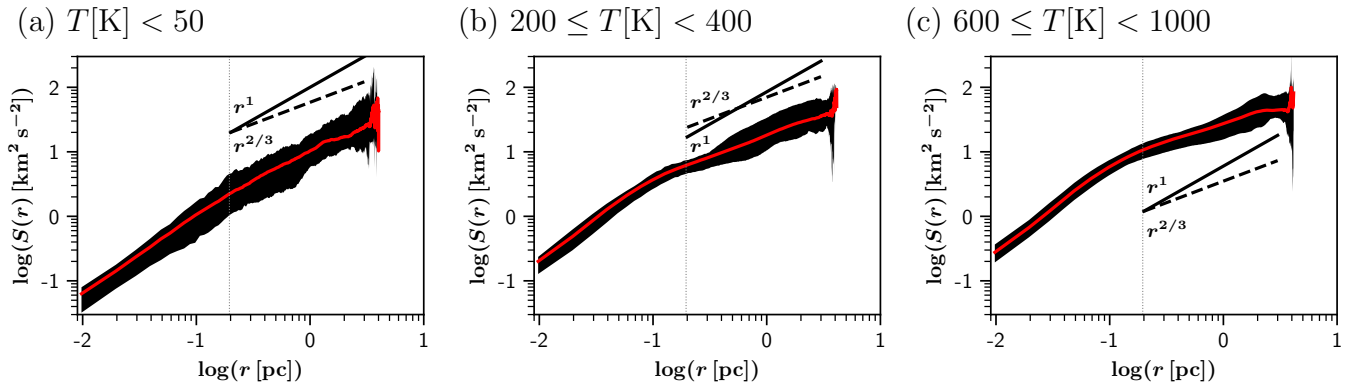


**Figure 8.** The second-order velocity function  $S(r)$  averaged over the nine sub-volumes. Each panel corresponds to the temperature thresholds of (a)  $T[\text{K}] < 50$ , (b)  $200 \leq T[\text{K}] < 400$ , (c)  $600 \leq T[\text{K}] < 1000$  at 3 Myr. The black shade shows the range of the measured  $S(r)$  whereas the lines show the power-law function of Kolmogorov (dashed:  $S(r) \propto r^{2/3}$ ) and Larson (solid:  $S(r) \propto r^1$ ). The red line shows the mean of nine sub-volumes. We discuss the powers on  $r \gtrsim 0.2$  pc (shown as vertical gray dotted line), where the powers are free from the numerical diffusion (see Appendix A).

nal velocity dispersion of CNM clumps is 1.05, 1.02, and 1.44  $\text{km s}^{-1}$  when the spatial resolution is 0.01, 0.02, and 0.04 pc.

This convergence originates in the fact that the power of the internal turbulence is stronger on larger scales (as suggested in Panel (a) of Figure 8). This means that, in the evaluation of the velocity dispersion responsible for the density PDF, it is important to resolve the eddies whose sizes are close to CNM clumps' sizes. The CNM clumps' sizes ( $\sim 0.1$  pc) are typically comparable to the spatial scale at which the numerical diffusion starts to play in our current simulation ( $\sim 0.2$  pc). The structure function at 0.1 pc in Panel (a) is still close the continuation of the  $r^1$  scale-dependence from the larger scales, which is free from the numerical diffusion ( $\gtrsim 0.2$  pc). This suggests that the impact of the numerical diffusion is still limited for the turbulent eddy whose size is  $\sim 0.1$  pc.

Therefore, although it is still ideal to perform simulations with a higher spatial resolution to investigate more precise scale-dependence of the velocity dispersion within CNM clumps, we expect that such simulations do not significantly change our current conclusion that the internal velocity dispersion is important to control the density PDF rather than the inter-clump relative velocity. Our convergence study in Appendix A suggests that resolving the CNM clump size with  $\gtrsim 5$  cells is the typical criteria to have the convergence in CNM clump mean properties.

### 6.3. Caveats: Other conditions and physical processes

The flow velocity that we employ in the current simulations is  $20 \text{ km s}^{-1}$ , a typical velocity of the shock propagation at late stages of supernova remnant expansion.

However a faster velocity  $\gtrsim 100 \text{ km s}^{-1}$  also exists in galaxy-galaxy tidal interactions or mergers (e.g., Fukui et al. 2017; Maeda et al. 2021). Such fast flows generate stronger shear motion in the shock-compressed layer and can change the turbulent mode ratio and/or CNM mass fraction by preventing the thermal instability. This is beyond our scope in this article, but the dependence on flow velocity has to be investigated to understand more intense star-forming regions (c.f., Kim & Ryu 2005; Federrath & Klessen 2012, for the Mach number dependence of the velocity/density power spectrum and the density PDF).

Magnetic fields also play important roles in cloud formation and evolution through the magnetic pressure (e.g., Hennebelle & Pérouault 2000; Inoue & Inutsuka 2008; Heitsch et al. 2009; Inoue & Inutsuka 2012; Vázquez-Semadeni et al. 2011; Iwasaki et al. 2019) and the formation of filamentary structures that host protostar (André et al. 2010; Inoue & Fukui 2013). The thermal instability is able to grow along the magnetic field lines to form multiphase structure. For examples, Inoue & Inutsuka (2012) and Iwasaki et al. (2019) show that, even in magnetized cases, the converging flows are able to create highly turbulent two-phase molecular clouds like the results in this article, especially when the angle between the converging flow direction and magnetic fields is close to parallel. We therefore should investigate whether our understanding is valid in magnetohydrodynamics regime by comparing the known relation of the density PDF width in magnetized isothermal gas (e.g., Federrath & Klessen 2012). This is beyond the scope at this moment, but we are planning to extend our simulations towards this direction.

It is also important to calculate chemical networks (either on-the-fly or post-process) followed with a synthetic observation to directly compare with molecular line observations. The WNM and CNM volumes are, in principle, accessible by HI and CO line observations, whereas we expect that the intermediate temperature range of a few 100 K is an interesting frontier traceable by the combination of the OH lines (e.g., [Ebisawa et al. 2020](#)) and by the HI line, with ALMA, SKA, ngVLA and so on. Such calculations are left for future studies at this moment.

#### 6.4. Implications to Observational Estimations in Interstellar Solenoidal/Compressive Mode Ratio

Direct observations of the solenoidal/compressive mode ratio parameter  $b$  in actual molecular clouds are difficult because observations are limited to the position-velocity space. Nevertheless, there have been attempts to estimate the solenoidal/compressive mode ratio by using Equation 5 (or its magnetized version) based on the measured Mach number and the width of log-normal density PDF (e.g., [Brunt 2010](#); [Federrath et al. 2016](#); [Sharda et al. 2021](#)). For example, [Federrath et al. \(2016\)](#) find that typical molecular clouds have their  $b$  greater than 0.4, with a significant compressive mode contribution exceeding the natural mixing, whereas the G0.253+0.016 cloud at the Central Molecular Zone exhibits  $b = 0.22$ , dominated by the solenoidal modes. The authors suspect that the origin of this variation is in the difference of the driving mechanism; the strong shear motion is invoked by its recent galactic-pericenter passage by Sgr A\* ([Longmore et al. 2013a](#)), which explains the low star formation efficiency at the Galactic Center ([Longmore et al. 2013b](#)).

The exact value of  $b$ , however, needs careful analyses. For example, [Brunt \(2010\)](#) discuss how the sub-resolution structures below 0.1 pc impact the  $b$  estimation by assuming that the Larson’s law continues to the infinitely small spatial scale ([Heyer et al. 2001](#)), and conclude that such structures induce the underestimation in  $b$  by a factor of  $\sim \sqrt{2}$  in the case of the Taurus molecular cloud, and this has to be tested by observations with a higher angular resolution. Such sub-resolution effect is indeed important because the thermal instability grow on wide spatial ranges even below 0.1 pc ([Koyama & Inutsuka 2000](#)). Furthermore, even with a high angular resolution, observational estimations of the Mach number using molecular lines (e.g., CO, HNC, etc.) have a chance to probe the relative velocity between CNM clumps along the line of sight. This relative velocity is powered more by the strong turbulence of the WNM and UNM and does not determine the density PDF at the

CNM temperature/density. Therefore, to address the variation of the mode ratio parameter  $b$  across various star-forming environments, we have to take the multiphase nature of the ISM into account, by selecting the turbulent motion within the dense structures. Higher spectral resolution is important as well as higher spatial resolution (see also [Federrath 2013a](#) for the importance of the Mach number estimation as an origin of the variation in SFR at a given gas column density).

## 7. SUMMARY

Towards the understanding of the turbulence properties realized in the multiphase interstellar medium (ISM), we perform a series of hydrodynamics simulations of converging warm neutral medium (WNM) flows on a 10 pc scale with heating and cooling by which the thermally unstable neutral medium (UNM) and the clumpy cold neutral medium (CNM) form. We list our main findings as follows.

1. The overall velocity power spectrum follows the Kolmogorov law where the solenoidal (compressive) modes account for  $> 80\%$  ( $< 20\%$ ) of the turbulence power on all scales.
2. When we consider both the UNM and CNM components, the density probability distribution function (PDF) has its width,  $\sigma_s$ , close to the one expected from the framework of the isothermal turbulence theory as  $\sigma_{s,\text{theory}} = \ln(1 + b^2 \mathcal{M}^2)$  (where  $\mathcal{M}$  and  $b$  are the turbulent Mach number and the turbulence parameter representing the turbulence mode ratio, respectively). Meanwhile, the width of the CNM component alone is narrower than the width that the isothermal theory predicts, if the isothermal theory employs the inter-clump relative velocity between CNM clumps as the main driver of turbulence responsible to control the CNM density PDF.
3. These results suggest that the coldest part of the density PDF (i.e., clumpy CNM structures) is governed by the thermal instability and the resultant weak turbulence of  $\lesssim 1 \text{ km s}^{-1}$  within individual CNM clumps rather than by the strong turbulence on the entire cloud scale with  $2 - 5 \text{ km s}^{-1}$ , which determines the relative velocity between CNM clumps. Observational interpretations of the CNM density PDF requires careful analyses to evaluate the turbulence within each CNM clump but not the relative velocity between CNM clumps; otherwise the Mach number of the turbulence can be overestimated and the corresponding forcing parameter  $b$  is underestimated

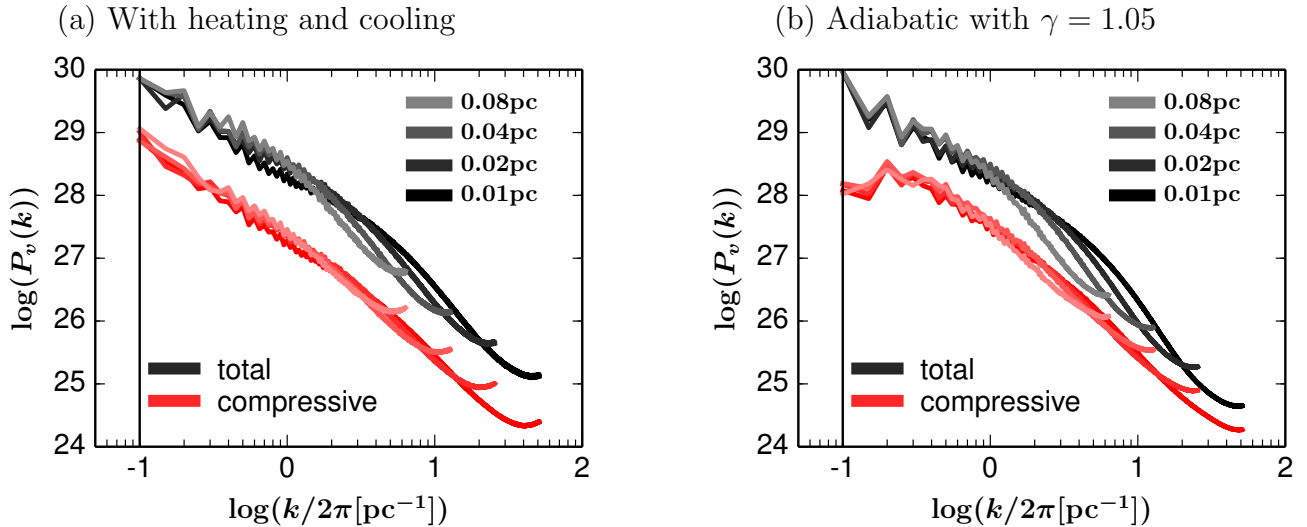


**Figure 9.** The velocity power spectrum for our fiducial calculation with heating and cooling (Panel (a)), and that for our reference calculation with adiabatic converging flow of  $\gamma = 1.05$  (Panel (b)). The black lines represent the total power and the red lines represent the power of the compressive mode. The four lines correspond to the spatial resolution of 0.08 pc, 0.04 pc, 0.02 pc, and 0.01 pc. For the visualization purpose, we do not plot the solenoidal modes here, whose power is almost same as the total power. Panel (a) is at 3 Myr, whereas Panel (b) is at 1.5 Myr; the shock-compressed layer hits the  $x$ -boundaries at  $\simeq 2$  Myr in the adiabatic case, so that for Panel (b) we choose the snapshot early enough to avoid the effect of the boundary.

accordingly.  $\sigma_{s,\text{theory}}$  is indeed close to  $\sigma_s$ , when the isothermal theory uses ~~we use~~ the mean Mach number of the internal turbulence within CNM clumps to derive  $\sigma_{s,\text{theory}}$ .

4. The second-order velocity structure function suggests that the overall volume follows the Kolmogorov spectrum, as already shown by Figure 2, and that the limited volume of the CNM component alone follows more to the Larson's spectrum. If we observationally measure the density PDF and the second-order velocity structure function in multiple thermal states, they provide estimations of the turbulent forcing parameter  $b$  more consistent with the thermal evolution of molecular clouds.
5. Our resolution study suggests that resolving the CNM clump size with  $\gtrsim 5$  cells is the typical criteria to have the convergence in the mean properties of CNM clumps.

These results have to be further investigated by including magnetic fields. We also hope that upcom-

ing observations (e.g., ALMA, SKA, ngVLA) measure the UNM/CNM (column) density PDF and the velocity structure function with multiple lines (HI, OH, CO) to investigate our results.

#### ACKNOWLEDGMENTS

Numerical computations were carried out on Cray XC30 and XC50 at Center for Computational Astrophysics, National Astronomical Observatory of Japan. MINK (15J04974, 18J00508, 20H04739), TI (18H05436, 20H01944), KT (16H05998, 16K13786, 17KK0091, 21H04487), and KI (19K03929, 19H01938), are supported by Grants-in-Aid from the Ministry of Education, Culture, Sports, Science, and Technology of Japan. MINK appreciate Atsushi J. Nishizawa and Chiaki Hikage for helping our Fourier analysis. MINK is grateful to Tomoaki Matsumoto, Kazuyuki Omukai, Hajime Susa, Sho Higashi, Gen Chiaki, Hajime Fukushima, Shuichiro Inutsuka, Shinsuke Takasao, Tetsuo Hasegawa, and Kengo Tachihara for fruitful comments. We are grateful to Hiroki Nakatsugawa who contributed the early phase of this study through his master thesis work.

#### APPENDIX

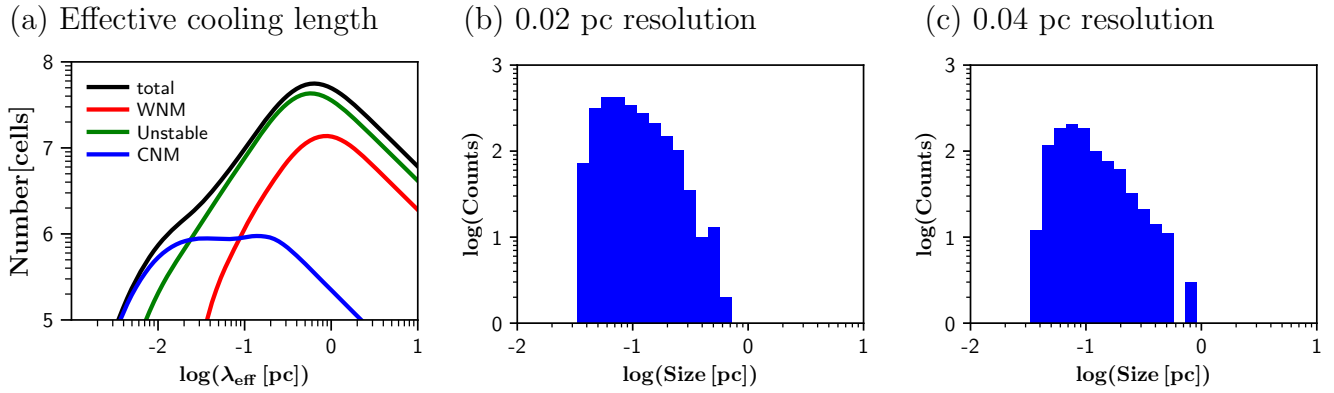


**Figure 10.** Panel (a): The histogram of the effective cooling length  $\lambda_{\text{cool,eff}} = eC_s/(\rho\mathcal{L} + P\nabla_i\mathbf{v}_i)$  at 3 Myr. The black shows the total histogram whereas the red/green/blue lines represent the histogram of the WNM/UNM/CNM. Panels (b) and (c): The CNM clump size histogram with 0.02 pc spatial resolution (b) and with 0.04 pc spatial resolution (c).

### A. NUMERICAL DIFFUSION AND IDEAL SPATIAL RESOLUTION

As shown in Section 4.1, the turbulence power spectrum exhibits a break at an intermediate spatial scale of  $k/2\pi \sim 5.12 \text{ pc}^{-1}$ . Such a break widely appears in various previous simulations as well, which is likely due to numerical diffusion; e.g., Federrath 2013b; Padoan et al. 2016; also Hennebelle & Audit 2007 (high-resolution albeit two-dimensional). To investigate the possible responsibility of the numerical diffusion, we perform additional simulations with multiple resolutions and compare the velocity power spectrum, which is shown in Figure 9. Panel (a) shows the spectrum from fiducial runs with multiple spatial resolutions and Panel (b) shows the spectrum from reference runs where we calculate the adiabatic converging flows with the specific heat ratio of 1.05. The choice of 1.05 here aims to investigate the evolution of the almost isothermal ISM, free from the heating and cooling effect. These panels show that the break scale shifts at about one-tenth of the Nyquist frequency as we change the spatial resolution, suggesting that this decrease of the turbulence power at high frequencies is due to the numerical diffusion. The relative increase of the compressive modes below this break scale is due to the numerical diffusion accordingly. We therefore employ powers above this break scale to evaluate the turbulence mode ratio  $\chi$  and the forcing parameter  $b$ . For example, when we analyze the entire volume of the shock-compressed layer in Section 4, we integrate the turbulence power from  $k/2\pi = 0.1$  to  $5.12 \text{ pc}^{-1}$ . Note that, in general, resolving vortex motions likely requires more numerical cells than resolving contracting/expanding motions so that the solenoidal modes tend to lose its power than the compressive mode.

In our previous study (Kobayashi et al. 2020), we show that our current spatial resolution of 0.01 pc is already high enough compared with the typical cooling length of the UNM  $\sim 1 \text{ pc}$  and it is capable of following the dynamical condensation motion from the UNM to the CNM due to the thermal instability. Indeed Kobayashi et al. (2020) show that the CNM mass fraction is converged with the spatial resolution of 0.02 pc or higher. Panel (a) of Figure 10 shows the histogram of the effective cooling length  $\lambda_{\text{cool,eff}}$  in our current simulation, where we calculate  $\lambda_{\text{cool,eff}} = eC_s/(\rho\mathcal{L} + P\nabla_i\mathbf{v}_i)$  in each numerical cell. The transition from the WNM to CNM appears at  $\sim 0.1 \text{ pc}$ , which is consistent with the peak of CNM clumps' sizes in Panel (a) of Figure 5. Panel (a) of Figure 10 suggests that the spatial resolution of 0.01 pc is a scale where the CNM dominates the cooling length. This panel also suggests that the largest scale of the numerical diffusion ( $\sim 0.2 \text{ pc}$ ) resolves the typical cooling length of the UNM ( $\sim 1 \text{ pc}$ ), and is close to the transition from the WNM to CNM. Therefore, our current simulations indeed follow the dynamical condensation motion from the WNM/UNM to the CNM.

Our current 0.01 pc resolution, however, limits the highest frequency mode of the thermal instability growth. CNM clumps are typically resolved with 10 cells per dimension (i.e.,  $0.1 \text{ pc} / 0.01 \text{ pc}$ ), thus it is difficult to follow the detailed evolution of the turbulent structure within individual clumps. In a self-gravitating system where the gravitational collapse enhances the turbulence, resolving the Jeans length by more than 32 cells is suggested as the criteria to have the convergence in the turbulent power of the solenoidal modes (e.g., Federrath et al. 2011; Higashi et al. 2021). Our simulations presented in this article do not include self-gravity but include heating/cooling processes, which invoke the dynamical condensation motion by the thermal instability and resultant turbulence on smallest scales. The gas temperature decreases during this condensation motion so that the 32-cell Jeans criterion of isothermal collapsing

**Table 3.** Resolution dependence of the CNM clump properties

| Resolution [pc]  | 0.01 | 0.02 | 0.04 |
|--|------|------|------|
| Number of CNM clumps   | 2403 | 2360 | 1028 |
| $\langle n_{\text{clump}} \rangle_V$ [ $\text{cm}^{-3}$ ]  | 189  | 183  | 170  |
| $\langle C_{s,\text{clump}} \rangle_V$ [ $\text{km s}^{-1}$ ]  | 0.65 | 0.65 | 0.67 |
| $\sqrt{\langle (\delta v^2)_{\text{clump}} \rangle_V}$ [ $\text{km s}^{-1}$ ]  | 1.05 | 1.02 | 1.44 |
| $\mathcal{M}_{\text{clump}} = \sqrt{\langle (\delta v^2)_{\text{clump}} \rangle_V} / \langle C_{s,\text{clump}} \rangle_V$ | 1.61 | 1.57 | 2.15 |
| $f_{\langle (\nabla \cdot \mathbf{v})^2 \rangle}$ [%]  | 22.5 | 18.9 | 15.3 |
| $f_{\langle (\nabla \times \mathbf{v})^2 \rangle}$ [%]   | 77.5 | 81.1 | 84.7 |

**Note.** The top row: the spatial resolution and number of identified CNM clumps. The middle row: The first line,  $\langle n_{\text{clump}} \rangle_V$  shows the mean number density of a CNM clump. The second line,  $\langle C_{s,\text{clump}} \rangle_V$  corresponds to the mean sound speed of a CNM clump. The third line,  $\sqrt{\langle (\delta v^2)_{\text{clump}} \rangle_V}$ , corresponds to the mean internal velocity dispersion of a CNM clump. The fourth line,  $\mathcal{M}_{\text{clump}}$ , is the mean effective Mach number within CNM clumps. The fifth and sixth lines,  $f_{\langle (\nabla \cdot \mathbf{v})^2 \rangle}$  ( $f_{\langle (\nabla \times \mathbf{v})^2 \rangle}$ ), show the grid-scale fraction of compressive (solenoidal) mode out of the total turbulence power, based on the measurements of  $\langle (\nabla_{\mathbf{g}} \cdot \mathbf{v})^2_{\text{clump}} \rangle_V$  and  $\langle (\nabla_{\mathbf{g}} \times \mathbf{v})^2_{\text{clump}} \rangle_V$ .

gas is not directly applicable, but this criterion suggests that we ideally should have  $\sim 3 \times 10^{-3}$  pc or higher spatial resolution to fully resolve the turbulent motions within individual CNM clumps of  $\sim 0.1$  pc sizes. In our current simulations, the fastest growing mode of the thermal instability should exist at the scale  $\sim 7 \times 10^{-3}$  pc, based on the typical sound speed ( $0.65 \text{ km s}^{-1}$ ) and the cooling time (0.011 Myr) of CNM clumps with 40 K and  $189 \text{ cm}^{-3}$ . The spatial resolution  $\lesssim 3 \times 10^{-3}$  pc is, therefore, desired to fully follow the formation of tiny CNM clumps or tiny structure within CNM clumps on the scale of  $\sim 7 \times 10^{-3}$  pc. Such a high resolution simulation is difficult to perform in three dimension unless we ignore the cloud-scale evolution  $\sim 10$  pc (i.e., WNM and UNM components) and focus on local structures within molecular clouds, which is left for future studies.

Nevertheless, the mass spectrum in Panel (b) of Figure 5 shows that the CNM mass budget is dominated by massive/large clumps so is the density PDF. This is consistent with theoretically expected mass spectrum under the thermal instability (Hennebelle & Audit 2007) and we expect that this spectrum is maintained even in simulations with much higher spatial resolutions. Therefore, our current simulations already measure the turbulence most responsible for the density PDF, which are eddies on the CNM clump scale (see Section 6.2). In addition, we perform the CNM clump identification on the reference runs with the spatial resolution with 0.02 pc and 0.04 pc. The minimum number of member cells is 64 cells (8 cells) for 0.02 pc (0.04 pc) resolutions, scaled with the resolution. Table 3 shows the measured CNM clump properties. These results show that physical properties of the CNM clumps as well as the grid-scale ratio of the turbulence mode start to have convergence with  $\lesssim 0.02$  pc resolution. This suggests that resolving the CNM clump size with  $\gtrsim 5$  cells (i.e., 0.1 pc / 0.02 pc) is a typical criteria to have the convergence in CNM clump mean properties.

## B. ASSUMPTIONS IN THE FOURIER TRANSFORMATION AND TECHNICAL PROCEDURES TO DERIVE THE POWER SPECTRUM

In the evaluation of the mode ratio  $\chi$  and the forcing parameter  $b$ , we choose one-tenth of the Nyquist frequency as the highest frequency (i.e.,  $k/2\pi = 5.12 \text{ pc}^{-1}$ ), below which is the turbulent inertial range. Meanwhile, the choice of the lowest frequency and the estimation of corresponding power on that scale is not trivial. In this section, we summarize the assumptions and the technical procedures involved in these analyses.

### B.1. The Frequency Range: Entire Shock-Compressed Layer

As already shown in Figure 1, the shock-compressed layer is significantly deformed, which evolves in time, and thus performing the Fourier transformation on such an arbitrary volume is not trivial. Ideally we should apply some methods to remove the effect of such geometry. There are already several methods proposed in astrophysical context, such as the Cosmic Microwave Background analysis whose mask region onto the galactic foreground has the complicated shapes (e.g., Planck Collaboration et al. 2014), or such as large galactic surveys where the observed area does not have any



periodicity (e.g., Pseudo-spectrum method; Brown et al. 2005; Hikage et al. 2011, 2019). However, these high accuracy is beyond our scope at this moment.

We instead opt to fill the velocity fields outside the shock-compressed layer uniformly by the mean bulk velocity of the shock-compressed layer, so that the power of low frequencies are reduced, which are otherwise dominated by the converging flow itself. The converging flow configuration naturally results in the mean bulk velocity of the shock-compressed layer as 0 (in other words, the shock-compressed layer is by definition in the rest-frame of the contact discontinuity). We therefore use  $\mathbf{v} = 0$  as this temporally filling velocity outside the shock-compressed layer and perform the Fourier transform over the entire simulation domain. Before the actual applications, we perform simple demonstrations. We first generate turbulence of solenoidal-mode-only (compressive-mode-only) in  $10 \text{ pc} \times 10 \text{ pc} \times 10 \text{ pc}$  domain by superposing 32 sinusoidal modes with the Kolmogorov power spectrum. We locate this velocity field at the center of  $20 \text{ pc} \times 10 \text{ pc} \times 10 \text{ pc}$  domain with the velocity field outside the central  $(10 \text{ pc})^3$  be 0. We perform the Fourier transform over the entire volume of  $20 \text{ pc} \times 10 \text{ pc} \times 10 \text{ pc}$  domain and found that the power on the  $k/2\pi = 1/20 \text{ pc}^{-1}$  scale is successfully suppressed more than one order of magnitude than the power on the  $k/2\pi = 1/10 \text{ pc}^{-1}$  scale, and obtain the Kolmogorov power spectrum where the artificial mode conversion due to the  $\mathbf{v} = 0$  procedure is limited to  $\lesssim 5$  percent.

In actual calculations, the shock-compressed layer is significantly deformed and is not as simple as our test calculations. Nevertheless, the physical width of the shock-compressed layer is 10–12 pc after 1 Myr and the mean bulk velocity of the shock-compressed layer is limited to  $< 1 \text{ km s}^{-1}$ , at least one order of magnitude smaller than the turbulent velocity. We therefore use this method in our analysis and employ  $k/2\pi = 0.1 \text{ pc}^{-1}$  as the proxy of the lowest frequency representing the shock-compressed layer throughout this article (e.g., when we measure  $\chi$  and  $b$ ).

### B.2. The Frequency Range: Sub-Volumes

In case of the Fourier analysis of the sub-volumes, we always set the lowest frequency as the frequency corresponds to 2.56 pc because we analyze the cubic of  $(2.56 \text{ pc})^3$ . We here did not apply any spacial care of  $\mathbf{v} = 0$  as we did above in Section B.1. This fixed volume and fixed frequency range affect the large scatter in the mode ratio among these sub-volumes at early stages (Panel (b) of Figure 6). Each sub-volume has the different timing at which they become completely embedded within the shock-compressed layer. The layer initially expands almost adiabatically with its width to 2 pc at 0.5 Myr, then the expansion gradually slows down due to the cooling with the width to 8 pc at 1 Myr, which corresponds to the separation between the most-separated sub-volumes. Therefore, it is fair to focus on the evolution of after 1 Myr when we discuss the variation among the sub-volumes, and we report most of our results from 3 Myr in Section 5.

## REFERENCES

- Alves de Oliveira, C., Schneider, N., Merín, B., et al. 2014, A&A, 568, A98, doi: [10.1051/0004-6361/201423504](https://doi.org/10.1051/0004-6361/201423504)
- André, P., Men'shchikov, A., Bontemps, S., et al. 2010, A&A, 518, L102, doi: [10.1051/0004-6361/201014666](https://doi.org/10.1051/0004-6361/201014666)
- Armstrong, J. W., Rickett, B. J., & Spangler, S. R. 1995, ApJ, 443, 209, doi: [10.1086/175515](https://doi.org/10.1086/175515)
- Audit, E., & Hennebelle, P. 2005, A&A, 433, 1, doi: [10.1051/0004-6361:20041474](https://doi.org/10.1051/0004-6361:20041474)
- Balbus, S. A. 1986, ApJL, 303, L79, doi: [10.1086/184657](https://doi.org/10.1086/184657)
- . 1995, ApJ, 453, 380, doi: [10.1086/176397](https://doi.org/10.1086/176397)
- Brown, M. L., Castro, P. G., & Taylor, A. N. 2005, MNRAS, 360, 1262, doi: [10.1111/j.1365-2966.2005.09111.x](https://doi.org/10.1111/j.1365-2966.2005.09111.x)
- Brunt, C. M. 2010, A&A, 513, A67, doi: [10.1051/0004-6361/200913506](https://doi.org/10.1051/0004-6361/200913506)
- Carroll-Nellenback, J. J., Frank, A., & Heitsch, F. 2014, ApJ, 790, 37, doi: [10.1088/0004-637X/790/1/37](https://doi.org/10.1088/0004-637X/790/1/37)
- Cox, D. P., & Tucker, W. H. 1969, ApJ, 157, 1157, doi: [10.1086/150144](https://doi.org/10.1086/150144)
- Dalgarno, A., & McCray, R. A. 1972, ARA&A, 10, 375, doi: [10.1146/annurev.aa.10.090172.002111](https://doi.org/10.1146/annurev.aa.10.090172.002111)
- Ebisawa, Y., Sakai, N., Menten, K. M., Oya, Y., & Yamamoto, S. 2020, ApJ, 904, 136, doi: [10.3847/1538-4357/abc16f](https://doi.org/10.3847/1538-4357/abc16f)
- Elmegreen, B. G., & Scalo, J. 2004, ARA&A, 42, 211, doi: [10.1146/annurev.astro.41.011802.094859](https://doi.org/10.1146/annurev.astro.41.011802.094859)
- Federrath, C. 2013a, MNRAS, 436, 3167, doi: [10.1093/mnras/stt1799](https://doi.org/10.1093/mnras/stt1799)
- . 2013b, MNRAS, 436, 1245, doi: [10.1093/mnras/stt1644](https://doi.org/10.1093/mnras/stt1644)
- Federrath, C., & Klessen, R. S. 2012, ApJ, 761, 156, doi: [10.1088/0004-637X/761/2/156](https://doi.org/10.1088/0004-637X/761/2/156)
- Federrath, C., Klessen, R. S., & Schmidt, W. 2008, ApJL, 688, L79, doi: [10.1086/595280](https://doi.org/10.1086/595280)

- Federrath, C., Roman-Duval, J., Klessen, R. S., Schmidt, W., & Mac Low, M. M. 2010, *A&A*, 512, A81, doi: [10.1051/0004-6361/200912437](https://doi.org/10.1051/0004-6361/200912437)
- Federrath, C., Sur, S., Schleicher, D. R. G., Banerjee, R., & Klessen, R. S. 2011, *ApJ*, 731, 62, doi: [10.1088/0004-637X/731/1/62](https://doi.org/10.1088/0004-637X/731/1/62)
- Federrath, C., Rathborne, J. M., Longmore, S. N., et al. 2016, *ApJ*, 832, 143, doi: [10.3847/0004-637X/832/2/143](https://doi.org/10.3847/0004-637X/832/2/143)
- Field, G. B. 1965, *ApJ*, 142, 531, doi: [10.1086/148317](https://doi.org/10.1086/148317)
- Frigo, M., & Johnson, S. G. 2005, *Proceedings of the IEEE*, 93, 216
- Fukui, Y., Tsuge, K., Sano, H., et al. 2017, *PASJ*, 69, L5, doi: [10.1093/pasj/psx032](https://doi.org/10.1093/pasj/psx032)
- Fukushima, H., & Yajima, H. 2021, arXiv e-prints, arXiv:2104.10892. <https://arxiv.org/abs/2104.10892>
- Fukushima, H., Yajima, H., Sugimura, K., et al. 2020, *MNRAS*, 497, 3830, doi: [10.1093/mnras/staa2062](https://doi.org/10.1093/mnras/staa2062)
- Heitsch, F., Stone, J. M., & Hartmann, L. W. 2009, *ApJ*, 695, 248, doi: [10.1088/0004-637X/695/1/248](https://doi.org/10.1088/0004-637X/695/1/248)
- Hennebelle, P., & Audit, E. 2007, *A&A*, 465, 431, doi: [10.1051/0004-6361:20066139](https://doi.org/10.1051/0004-6361:20066139)
- Hennebelle, P., & Pérault, M. 2000, *A&A*, 359, 1124
- Heyer, M. H., & Brunt, C. M. 2004, *ApJL*, 615, L45, doi: [10.1086/425978](https://doi.org/10.1086/425978)
- Heyer, M. H., Carpenter, J. M., & Snell, R. L. 2001, *ApJ*, 551, 852, doi: [10.1086/320218](https://doi.org/10.1086/320218)
- Higashi, S., Susa, H., & Chiaki, G. 2021, arXiv e-prints, arXiv:2105.07701. <https://arxiv.org/abs/2105.07701>
- Hikage, C., Takada, M., Hamana, T., & Spergel, D. 2011, *MNRAS*, 412, 65, doi: [10.1111/j.1365-2966.2010.17886.x](https://doi.org/10.1111/j.1365-2966.2010.17886.x)
- Hikage, C., Oguri, M., Hamana, T., et al. 2019, *PASJ*, 71, 43, doi: [10.1093/pasj/psz010](https://doi.org/10.1093/pasj/psz010)
- Hosokawa, T., & Inutsuka, S.-i. 2006, *ApJL*, 648, L131, doi: [10.1086/507887](https://doi.org/10.1086/507887)
- Inoue, T., & Fukui, Y. 2013, *ApJL*, 774, L31, doi: [10.1088/2041-8205/774/2/L31](https://doi.org/10.1088/2041-8205/774/2/L31)
- Inoue, T., & Inutsuka, S.-i. 2008, *ApJ*, 687, 303, doi: [10.1086/590528](https://doi.org/10.1086/590528)
- . 2012, *ApJ*, 759, 35, doi: [10.1088/0004-637X/759/1/35](https://doi.org/10.1088/0004-637X/759/1/35)
- Iwasaki, K., Tomida, K., Inoue, T., & Inutsuka, S.-i. 2019, *ApJ*, 873, 6, doi: [10.3847/1538-4357/ab02ff](https://doi.org/10.3847/1538-4357/ab02ff)
- Kawamura, A., Mizuno, Y., Minamidani, T., et al. 2009, *ApJS*, 184, 1, doi: [10.1088/0067-0049/184/1/1](https://doi.org/10.1088/0067-0049/184/1/1)
- Kennicutt, R. C., & Evans, N. J. 2012, *ARA&A*, 50, 531, doi: [10.1146/annurev-astro-081811-125610](https://doi.org/10.1146/annurev-astro-081811-125610)
- Kida, S., & Orszag, S. A. 1990a, *Journal of Scientific Computing*, 5, 1
- . 1990b, *Journal of Scientific Computing*, 5, 85
- Kim, J., & Ryu, D. 2005, *ApJL*, 630, L45, doi: [10.1086/491600](https://doi.org/10.1086/491600)
- Kim, J.-G., Kim, W.-T., & Ostriker, E. C. 2018, *ApJ*, 859, 68, doi: [10.3847/1538-4357/aabe27](https://doi.org/10.3847/1538-4357/aabe27)
- Kim, J.-G., Ostriker, E. C., & Filippova, N. 2021, *ApJ*, 911, 128, doi: [10.3847/1538-4357/abe934](https://doi.org/10.3847/1538-4357/abe934)
- Klessen, R. S. 2000, *ApJ*, 535, 869, doi: [10.1086/308854](https://doi.org/10.1086/308854)
- Kobayashi, M. I. N., Inoue, T., Inutsuka, S.-i., et al. 2020, *ApJ*, 905, 95, doi: [10.3847/1538-4357/abc5be](https://doi.org/10.3847/1538-4357/abc5be)
- Kolmogorov, A. 1941, *Akademiia Nauk SSSR Doklady*, 30, 301
- Körtgen, B., Federrath, C., & Banerjee, R. 2017, *MNRAS*, 472, 2496, doi: [10.1093/mnras/stx2208](https://doi.org/10.1093/mnras/stx2208)
- Koyama, H., & Inutsuka, S.-i. 2000, *ApJ*, 532, 980, doi: [10.1086/308594](https://doi.org/10.1086/308594)
- Koyama, H., & Inutsuka, S.-i. 2002, *ApJL*, 564, L97, doi: [10.1086/338978](https://doi.org/10.1086/338978)
- Kruijssen, J. M. D., Schrubba, A., Chevance, M., et al. 2019, *Nature*, 569, 519, doi: [10.1038/s41586-019-1194-3](https://doi.org/10.1038/s41586-019-1194-3)
- Krumholz, M. R., & McKee, C. F. 2005, *ApJ*, 630, 250, doi: [10.1086/431734](https://doi.org/10.1086/431734)
- Larson, R. B. 1981, *MNRAS*, 194, 809, doi: [10.1093/mnras/194.4.809](https://doi.org/10.1093/mnras/194.4.809)
- Li, P. S., McKee, C. F., Klein, R. I., & Fisher, R. T. 2008, *ApJ*, 684, 380, doi: [10.1086/589874](https://doi.org/10.1086/589874)
- Lombardi, M., Alves, J., & Lada, C. J. 2011, *A&A*, 535, A16, doi: [10.1051/0004-6361/201116915](https://doi.org/10.1051/0004-6361/201116915)
- . 2015, *A&A*, 576, L1, doi: [10.1051/0004-6361/201525650](https://doi.org/10.1051/0004-6361/201525650)
- Longmore, S. N., Kruijssen, J. M. D., Bally, J., et al. 2013a, *MNRAS*, 433, L15, doi: [10.1093/mnras/slt048](https://doi.org/10.1093/mnras/slt048)
- Longmore, S. N., Bally, J., Testi, L., et al. 2013b, *MNRAS*, 429, 987, doi: [10.1093/mnras/sts376](https://doi.org/10.1093/mnras/sts376)
- Maeda, R., Inoue, T., & Fukui, Y. 2021, *ApJ*, 908, 2, doi: [10.3847/1538-4357/abcc75](https://doi.org/10.3847/1538-4357/abcc75)
- Matsumoto, T., Dobashi, K., & Shimoikura, T. 2015, *ApJ*, 801, 77, doi: [10.1088/0004-637X/801/2/77](https://doi.org/10.1088/0004-637X/801/2/77)
- McKee, C. F., & Ostriker, J. P. 1977, *ApJ*, 218, 148, doi: [10.1086/155667](https://doi.org/10.1086/155667)
- Meidt, S. E., Hughes, A., Dobbs, C. L., et al. 2015, *ApJ*, 806, 72, doi: [10.1088/0004-637X/806/1/72](https://doi.org/10.1088/0004-637X/806/1/72)
- Nordlund, Å. K., & Padoan, P. 1999, in *Interstellar Turbulence*, ed. J. Franco & A. Carraminana, 218. <https://arxiv.org/abs/astro-ph/9810074>
- Padoan, P., & Nordlund, Å. 2002, *ApJ*, 576, 870, doi: [10.1086/341790](https://doi.org/10.1086/341790)
- . 2011, *ApJ*, 730, 40, doi: [10.1088/0004-637X/730/1/40](https://doi.org/10.1088/0004-637X/730/1/40)
- Padoan, P., Nordlund, A., & Jones, B. J. T. 1997, *MNRAS*, 288, 145, doi: [10.1093/mnras/288.1.145](https://doi.org/10.1093/mnras/288.1.145)
- Padoan, P., Pan, L., Haugbølle, T., & Nordlund, Å. 2016, *ApJ*, 822, 11, doi: [10.3847/0004-637X/822/1/11](https://doi.org/10.3847/0004-637X/822/1/11)
- Pan, L., Padoan, P., Haugbølle, T., & Nordlund, Å. 2016, *ApJ*, 825, 30, doi: [10.3847/0004-637X/825/1/30](https://doi.org/10.3847/0004-637X/825/1/30)

- Parker, E. N. 1953, *ApJ*, 117, 431, doi: [10.1086/145707](https://doi.org/10.1086/145707)
- Passot, T., & Vázquez-Semadeni, E. 1998, *PhRvE*, 58, 4501, doi: [10.1103/PhysRevE.58.4501](https://doi.org/10.1103/PhysRevE.58.4501)
- Planck Collaboration, Ade, P. A. R., Aghanim, N., et al. 2014, *A&A*, 571, A23, doi: [10.1051/0004-6361/201321534](https://doi.org/10.1051/0004-6361/201321534)
- Scalo, J., Vázquez-Semadeni, E., Chappell, D., & Passot, T. 1998, *ApJ*, 504, 835, doi: [10.1086/306099](https://doi.org/10.1086/306099)
- Schneider, N., André, P., Könyves, V., et al. 2013, *ApJL*, 766, L17, doi: [10.1088/2041-8205/766/2/L17](https://doi.org/10.1088/2041-8205/766/2/L17)
- Schneider, N., Bontemps, S., Motte, F., et al. 2016, *A&A*, 587, A74, doi: [10.1051/0004-6361/201527144](https://doi.org/10.1051/0004-6361/201527144)
- Seifried, D., Walch, S., Haid, S., Girichidis, P., & Naab, T. 2018, *ApJ*, 855, 81, doi: [10.3847/1538-4357/aaacff](https://doi.org/10.3847/1538-4357/aaacff)
- Sharda, P., Menon, S. H., Federrath, C., et al. 2021, *MNRAS*, doi: [10.1093/mnras/stab3048](https://doi.org/10.1093/mnras/stab3048)
- van Leer, B. 1979, *Journal of Computational Physics*, 32, 101, doi: [10.1016/0021-9991\(79\)90145-1](https://doi.org/10.1016/0021-9991(79)90145-1)
- Vázquez-Semadeni, E., Banerjee, R., Gómez, G. C., et al. 2011, *MNRAS*, 414, 2511, doi: [10.1111/j.1365-2966.2011.18569.x](https://doi.org/10.1111/j.1365-2966.2011.18569.x)